Geophysical Journal International

Geophys. J. Int. (2026) **245,** 1–17
Advance Access publication 2026 January 23
Research Paper

https://doi.org/10.1093/gji/ggag031

Numerical wavefield simulations with instantaneous time mirror in a 3-D elastic medium

V. Kurapati [1], G. Hillers [2], L. Krenz [1], A.-A. Gabriel [3,4] and M. Bader [1]

[1] *TUM School of Computation, Information and Technology, Technical University of Munich, 85748 Garching bei München, Germany. E-mail: vikas.kurapati@tum.de*
[2] *Institute of Seismology, Department of Geosciences and Geography, University of Helsinki, 00014 Helsinki, Finland*
[3] *Scripps Institution of Oceanography, University of San Diego, 92093 La Jolla, CA, USA*
[4] *Department of Earth and Environmental Sciences, Ludwig-Maximilians-University of Munich, 80333 Munich, Germany*

Accepted 2026 January 20. Received 2025 December 17; in original form 2025 July 24

SUMMARY

We simulate an instantaneous time mirror (ITM), that is, a rapid short-duration change in elastic material properties, using numerical experiments in time-varying isotropic elastic media. Our implementation in the seismic wave propagation software SeisSol is based on high-order discontinuous Galerkin discretization with ADER time stepping. We develop an eigenvector-based analytical solution for time interfaces for general linear hyperbolic wave systems and apply it to analyse the energy balance at time boundaries and ITMs. The energy increases for all intermittent medium changes for all impedance scaling factors. Our numerical implementation is validated against these analytical solutions and achieves high-order convergence. Its accuracy is further corroborated by estimates of reflection and transmission coefficients and observed frequency shifts across time boundaries, and by acoustic wave speed estimates obtained from focal spots associated with ITM-generated converging *P* waves that are consistent with theoretical predictions and ground truth values, respectively. We use the ITM implementation to simulate the partitioning of seismic body waves excited by a point source in a spatially homogeneous elastic full space. The response to an intermittent short change in the elastic parameters yields a diverging and converging *P* and *S* wavefield. A systematic scaling of the elastic parameters is then used to steer independent ITM reflections of either *P* or *S* waves. Numerical ITM solutions as developed here can be used to synthesize converging wavefields in seismic imaging applications, and more generally to analyse the behaviour and manipulation of seismic wavefields in space-time varying media.

Key words: Numerical modelling; Numerical solutions; Body waves; Computational seismology; Theoretical Seismology; Wave Propagation.

1 INTRODUCTION

Space and time play equally important roles in wave propagation. Thus, understanding the effects of space-varying and time-varying material properties on the wavefield is essential for many applications (K. Wapenaar *et al.* 2024; K. Wapenaar 2025). For seismic waves propagating in Earth, the impedance contrasts associated with layer boundaries and material changes (Fig. 1a) lead to well-studied phenomena that are important for our understanding of Earth structure. The space–time analogy (Fig. 1b) implies that reflections can also be caused by an interface or a disruption of material properties in time (K. Wapenaar *et al.* 2024; K. Wapenaar 2025). Intermittent, short-duration changes of the impedance-governing medium properties can lead to an instantaneous time mirror (ITM) (V. Bacot *et al.* 2016; M. Fink & E. Fort 2017), which creates time–boundary reflections by activating 'sources' everywhere in space (Fig. 1c).

Understanding the complex effects of space–time wavefield variations is essential for the manipulation of wavefields. ITM sources localized in time excite divergent and convergent waves just as material contrasts in space act as localized sources for transmitted and reflected waves (Fig. 1). Convergent waves excited by the ITM and by a classic time-reversal mirror (M. Fink 1997) demonstrate the time-reversal invariance property of the wave equation. However, in contrast to the functioning of a time-reversal mirror (M. Fink & E. Fort 2017) that records, stores, time-reverses and re-transmits a wave signal, the ITM does not involve an antenna of receiver–transmitter elements.

V. Bacot *et al.* (2016) developed a framework for explaining ITM effects that are based on the wave speed dependent

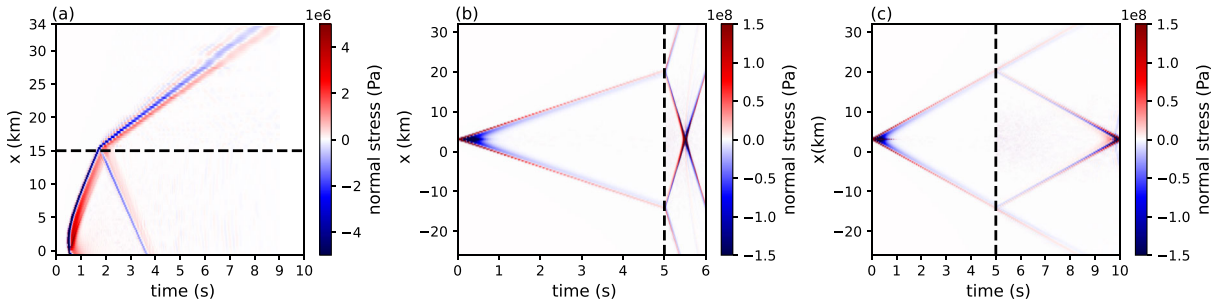

Figure 1. Space–time representations of 3-D simulated acoustic wavefields. All panels show the normal stress or pressure along the x-axis in response to a pressure impulse moment tensor point source. In each panel, the source and receiver configuration is adapted to demonstrate the responses. The dashed lines indicate the space and time interfaces. (a) Reflection and transmission at an impedance contrast or interface in space at $x = 15$ km. (b) Reflection and transmission at a single impedance contrast or interface in time at $t = 5$ s. (c) Reflection and transmission at an instantaneous time mirror (ITM) at $t = 5$ s. The ITM consists of two time interfaces separated by a very short interval τ.

coupling of the wavefield amplitude to its time derivative. A temporal wave speed disruption decouples the amplitude and its derivative and forms a new set of initial conditions that are controlled by the wavefield state in the entire medium at the instant of the mirror activation. This leads to a superposition of two decomposed states corresponding to the forward-propagating and backward-propagating waves. This manipulation retains a first-in-last-out symmetry (Fig. 1c) and thus differs from the reflections at boundaries in space (Fig. 1a) and at a time-reversal mirror with their first-in-first-out sequence. V. Bacot *et al.* (2016) first demonstrated the wave speed dependent ITM principle experimentally by disrupting the propagation of gravity water waves through an instantaneous acceleration, which intermittently changes the wave propagation speed in the medium due to its dependence on gravitational acceleration. Since then, time-dependent properties of various materials in different spectral bands have been manipulated to focus, shape and control the propagation of electromagnetic (V. Pacheco-Peña & N. Engheta 2020; C.T. Wu *et al.* 2022; E. Galiffi *et al.* 2023; R. Tirole *et al.* 2023), acoustic (B. Gérardin *et al.* 2019) and elastic waves (K. Innanen 2018).

The seismic wavefield anatomy can be controlled by manipulating active source properties, and specific source–receiver configurations can enhance target signals. In contrast, seismic metamaterials (A. Colombi *et al.* 2016; D. Mu *et al.* 2020) can passively influence the properties of an incident wavefield. A regular spatial configuration of resonators, including buildings (P. Guéguen *et al.* 2002), pile walls (A. Dijckmans *et al.* 2016), trenches (X. Pu & Z. Shi 2020), inclusions (A. Castanheira-Pinto *et al.* 2018), wind turbines (M. Pilz *et al.* 2024) and trees (P. Roux *et al.* 2018) can control the local wavefield, which has important implications for structural engineering, urban planning, seismic safety and hazard mitigation. Simulated time-reversed seismic wavefields are used for earthquake source characterization (A. Rietbrock & F. Scherbaum 1994; C. Larmat *et al.* 2006), and simulations are an essential element in adjoint imaging techniques for solving tomographic inverse problems (J. Tromp *et al.* 2005). The analogy between time-reversal and cross-correlation (A. Derode *et al.* 2003) explains the reconstruction of converging and diverging waves (N.M. Shapiro *et al.* 2005; F.-C. Lin *et al.* 2009; T. Gallot *et al.* 2011) and of spatial autocorrelation fields (G. Ekström *et al.* 2009; G. Hillers *et al.* 2016) from correlations of continuous seismic dense array records for passive surface wave imaging.

Reflectors in space and mirrors in time have been studied for wavefields in a range of materials (S. Catheline *et al.* 2008). The water wave experiment by V. Bacot *et al.* (2016) demonstrated that modifying the parameters that control the wave speed produces a time slab, or ITM. The properties of the propagation media in the solid Earth and its envelopes, including the hydrosphere, cryosphere and atmosphere, can experience sudden changes associated with natural and anthropogenic phenomena such as earthquakes, eruptions, collapses, explosions and injections. However, except for the numerical study of propagation in a 2-D elastic medium by K. Innanen (2018), the ITM response of a 3-D elastic or seismic wavefield is not analysed comprehensively.

In this work, we extend the numerical wave propagation code SeisSol (M. Dumbser & M. Käser 2006; M. Käser & M. Dumbser 2006; M. Dumbser *et al.* 2007a; M. Käser *et al.* 2010; L. Krenz *et al.* 2023; A.-A. Gabriel *et al.* 2025) with an implementation of ITM physics in elastic media to study the effects of space–time transformation on seismic wavefields. SeisSol has demonstrated its utility and performance in modelling earthquake scenarios with several billion degrees of freedom while achieving a significant fraction of the theoretical peak performance (A. Heinecke *et al.* 2014; C. Uphoff *et al.* 2017; L. Krenz *et al.* 2021). Our ITM implementation extends SeisSol's versatility to analyse a broader range of acoustic and elastic wave propagation phenomena (Fig. 1). We use SeisSol to manipulate the propagation of *P* waves and *S* waves simultaneously or separately, providing a tool and a basis for further investigations of seismic ITM effects.

In Section 2, we discuss the general wave equation and plane wave solutions using eigenvectors, introduce an analytical solution for the ITM disruption of an acoustic wave and discuss ITM physics for the elastic wave equation. We demonstrate the ITM implementation for the elastic case in SeisSol and perform a numerical convergence test in Section 3. In Section 4 we report the results from point source simulations for the acoustic case and the elastic case, before we discuss the implications for applications in Section 5.

2 PLANE WAVE SOLUTIONS IN RESPONSE TO TIME INTERFACES

2.1 Plane wave solution for the general wave equation with a time interface

In this work, a time interface activated at t_{int} is a step-function change in the material properties with respect to the previous state. The intermittently activated instantaneous time mirror

discussed in Sections 2.2 to 4 is a short sequence of two opposite step-function changes. This excludes more general time variations such as continuous, periodic or other transient components. We consider a general linear hyperbolic wave equation expressed in the first-order form

$$\frac{\partial \mathbf{q}}{\partial t} + \mathbf{A}\frac{\partial \mathbf{q}}{\partial x} + \mathbf{B}\frac{\partial \mathbf{q}}{\partial y} + \mathbf{C}\frac{\partial \mathbf{q}}{\partial z} = 0, \tag{1}$$

where the state vector $\mathbf{q}$ depends on time t and spatial directions x, y, z. The flux matrices in x, y, z are given by $\mathbf{A}$, $\mathbf{B}$, $\mathbf{C}$. Solutions to this system of constant-coefficient linear partial differential equations (PDEs) can be expressed as a linear summation of planar waves, similar to a Fourier basis decomposition (section 4.2.1 in L.C. Evans 2010). Using complex numbers, a plane wave with angular frequency ω and wavenumber k propagating in direction $\mathbf{n}$ can be written as

$$\mathbf{q}(\mathbf{x}, t) = \mathbf{r}\, e^{i(\omega t - k\mathbf{n}\cdot\mathbf{x})}, \tag{2}$$

where $\mathbf{x} = (x, y, z)$ and $\mathbf{n} = (n_1, n_2, n_3)$ is the unit vector that denotes the direction of propagation. Inserting eq. (2) into eq. (1), we obtain that the state vector $\mathbf{q}(\mathbf{x}, t)$ solves eq. (1) if

$$\underbrace{(\mathbf{A}n_1 + \mathbf{B}n_2 + \mathbf{C}n_3)}_{\hat{\mathbf{A}}}\mathbf{r} = \frac{\omega}{k}\mathbf{r}. \tag{3}$$

Thus, $\mathbf{r}$ needs to be an eigenvector of the plane wave operator $\hat{\mathbf{A}}$, where the wave speed $c = \omega/k$ is the corresponding eigenvalue. To formulate general solutions of the PDE system in eq. (1), we express the initial condition $\mathbf{q}(\mathbf{x}, 0)$ as a linear sum of eigenvectors with space-dependent functions, setting $t = 0$ in eq. (2)

$$\mathbf{q}(\mathbf{x}, 0) = \sum_j \mathbf{r}_j f_j(\mathbf{n}\cdot\mathbf{x}) = \sum_j \mathbf{r}_j e^{i(-k_j\mathbf{n}\cdot\mathbf{x})}, \tag{4}$$
$$f_j(\mathbf{n}\cdot\mathbf{x}) := e^{i(-k_j\mathbf{n}\cdot\mathbf{x})},$$

where $\mathbf{r}_j$ is the jth eigenvector and f_j is the component of the jth eigenvector in the linear split (R.J. LeVeque 2002, section 18.5). The plane wave solution of the PDE system in eq. (1) is then

$$\mathbf{q}(\mathbf{x}, t) = \sum_j \mathbf{r}_j f_j(\mathbf{n}\cdot\mathbf{x} - c_j t) = \sum_j \mathbf{r}_j e^{i(\omega_j t - k_j\mathbf{n}\cdot\mathbf{x})}, \tag{5}$$

where c_j is the jth eigenvalue, corresponding to the wave velocity.

The following discussion examines the plane wave solution with a single time interface. We distinguish two cases associated with constant and with changing eigenvectors, respectively. This can be related to the acoustic scenarios discussed in sections 9.7 and 9.8 in R.J. LeVeque (2002), where an invariant or a changing impedance between two domains with different wave speed and density are associated with a constant or varying eigenvector interface, respectively. The first invariant impedance interface is a tuned case where the wave speeds and densities differ but their product does not.

2.1.1 *Eigenvectors do not change at the time interface*

If the eigenvectors do not change at the time interface t_{int}, the new set of initial conditions is

$$\mathbf{q}(\mathbf{x}, t_{\text{int}}) = \sum_j \mathbf{r}_j f_j(\mathbf{n}\cdot\mathbf{x} - c_j t_{\text{int}}) = \sum_j \mathbf{r}_j e^{i(\omega_j t_{\text{int}} - k_j\mathbf{n}\cdot\mathbf{x})}, \tag{6}$$

which evolves in time according to

$$\begin{aligned}\mathbf{q}(\mathbf{x}, t) &= \sum_j \mathbf{r}_j f_j\big(\mathbf{n}\cdot\mathbf{x} - c_j t_{\text{int}} - \hat{c}_j(t - t_{\text{int}})\big) \\ &= \sum_j \mathbf{r}_j e^{i(\hat{\omega}_j(t - t_{\text{int}}) + \omega_j t_{\text{int}} - k\mathbf{n}\cdot\mathbf{x})}.\end{aligned} \tag{7}$$

Here, $\mathbf{r}_j$ is the jth eigenvector, f_j is the component of the jth eigenvector in the linear split and c_j is the jth eigenvalue. Correspondingly, $\hat{c}_j$ and $\hat{\omega}_j = k_j\hat{c}_j$ are the jth eigenvalue and the jth angular frequency after the material change, respectively. In this scenario, the wave components associated with different eigenvectors propagate without creating new components. However, if the eigenvalues vary, the velocities of the forward-moving waves change, which results in a phase shift. Consequently, the waves continue to travel faster or slower than the incident wave after the time interface.

2.1.2 *Eigenvectors change at the time interface*

If, on the other hand, the eigenvectors change in response to the material change at the time interface t_{int}, we split the new initial conditions

$$\mathbf{q}(\mathbf{x}, t_{\text{int}}) = \sum_j \mathbf{r}_j f_j\left(\mathbf{n}\cdot\mathbf{x} - c_j t_{\text{int}}\right) = \sum_i \hat{\mathbf{r}}_j \hat{f}_j(\mathbf{n}\cdot\mathbf{x}), \tag{8}$$

which evolves in time as

$$\mathbf{q}(\mathbf{x}, t) = \sum_j \hat{\mathbf{r}}_j \hat{f}_j\big(\mathbf{n}\cdot\mathbf{x} - \hat{c}_j(t - t_{\text{int}})\big), \tag{9}$$

where $\hat{\mathbf{r}}_j$ denotes the jth eigenvector after the material change, $\hat{f}_j$ denotes the space-dependent component of the jth eigenvector and $\hat{c}_j$ denotes the jth eigenvalue.

This shows that there can be components of different eigenvectors and eigenvalue pairs associated with the time interface. If, after the time interface, the decomposition of the new initial conditions creates eigenvectors that have paired negative and positive eigenvalues, it results in a reflected component in time. This is the case for the set of elastic wave equations analysed in Section 2.3.

If we consider a system with eigenvalues c and $-c$ and eigenvectors $\mathbf{r}_1$ and $\mathbf{r}_2$, the solution after the time interface, that is, the forward component, even if we begin with only one component, is

$$\mathbf{q}(\mathbf{x}, t_{\text{int}}) = \mathbf{r}_1 f_1(\mathbf{n}\cdot\mathbf{x} - c t_{\text{int}}) = \hat{\mathbf{r}}_1 \hat{f}_1(\mathbf{n}\cdot\mathbf{x}) + \hat{\mathbf{r}}_2 \hat{f}_2(\mathbf{n}\cdot\mathbf{x}), \tag{10}$$

which evolves in time as

$$\mathbf{q}(\mathbf{x}, t) = \hat{\mathbf{r}}_1 \hat{f}_1\big(\mathbf{n}\cdot\mathbf{x} - \hat{c}(t - t_{\text{int}})\big) + \hat{\mathbf{r}}_2 \hat{f}_2\big(\mathbf{n}\cdot\mathbf{x} + \hat{c}(t - t_{\text{int}})\big), \tag{11}$$

that is, a single component creates its reflection. Here $\hat{\mathbf{r}}_i$ is the eigenvector after the time interface, $\hat{f}_i$ is the component of the eigenvector $\hat{\mathbf{r}}_i$ and $\hat{c}$ is the eigenvalue of the solution after the time interface. In a scenario where the eigenvectors can be manipulated to affect only one component of the solution without modifying the other, only one component of the wavefield is reflected. This scenario is explored in Section 3.2 by manipulating elastic P waves and S waves independently.

If the initial eigenvalues are c_1 and c_2 with the corresponding eigenvalues $\hat{c}_1$ and $\hat{c}_2$ after the time interface, we obtain a solution that is similar to the result associated with a single initial eigenvector

$$\mathbf{q}(\mathbf{x}, t_{\text{int}}) = \mathbf{r}_1 f_1(\mathbf{n}\cdot\mathbf{x} - c_1 t_{\text{int}}) = \hat{\mathbf{r}}_1 \hat{f}_i(\mathbf{n}\cdot\mathbf{x}) + \hat{\mathbf{r}}_2 \hat{f}_2(\mathbf{n}\cdot\mathbf{x}), \quad (12)$$

$$\mathbf{q}(\mathbf{x}, t) = \hat{\mathbf{r}}_1 \hat{f}_i\big(\mathbf{n}\cdot\mathbf{x} - \hat{c}_1(t - t_{\text{int}})\big) + \hat{\mathbf{r}}_2 \hat{f}_2\big(\mathbf{n}\cdot\mathbf{x} - \hat{c}_2(t - t_{\text{int}})\big). \quad (13)$$

This result demonstrates that this combination of eigenvalues does not necessarily create a reflected component. In our analysis, we focus on scenarios where the eigenvectors change, which are associated with the conditions that control reflections at time boundaries.

2.2 Analytical solution for an acoustic plane wave in response to time interfaces and the energy balance

We discuss the analytical solution for an acoustic planar wavefield in response to a single time interface and an instantaneous time mirror. This analytical solution is used in Section 3.3 to corroborate the numerical implementation of the ITM in SeisSol. V. Bacot *et al.* (2016) defines an ITM as a sequence of time interfaces where the wave properties are changed intermittently for a very short duration τ. A corresponding analytical development for the elastic case is beyond the scope of this paper. As in Section 2.1, we work with a sinusoidal plane wave model. The set of acoustic wave equations in first-order hyperbolic form are defined as

$$\begin{aligned} \frac{\partial p}{\partial t} + \lambda \frac{\partial v_i}{\partial x_i} &= 0 \\ \rho \frac{\partial v_i}{\partial t} + \frac{\partial p}{\partial x_i} &= 0, \end{aligned} \quad (14)$$

where p is the pressure fluctuation, v_i are the particle velocities in the three directions, λ is the bulk modulus and ρ is the density. The sound wave speed in the acoustic medium is $c = \sqrt{\lambda/\rho}$. We next describe ITM-generated converging wavefield components in an acoustic 1-D system. We formulate eq. (14) in 1-D and analogous to eq. (1) as

$$\frac{\partial \mathbf{q}}{\partial t} + \mathbf{A}\frac{\partial \mathbf{q}}{\partial x} = 0 \qquad \text{or} \qquad \frac{\partial}{\partial t}\begin{pmatrix} p \\ v \end{pmatrix} + \begin{pmatrix} 0 & \lambda \\ \frac{1}{\rho} & 0 \end{pmatrix} \frac{\partial}{\partial x}\begin{pmatrix} p \\ u \end{pmatrix} = 0. \quad (15)$$

The eigenvalues for this system $c = \pm\sqrt{\lambda/\rho}$ exist in pairs and the eigenmatrix

$$\mathbf{R} = \begin{pmatrix} -\sqrt{\rho\lambda} & \sqrt{\rho\lambda} \\ 1 & 1 \end{pmatrix} \quad (16)$$

depends only on the material parameters λ and ρ. In the following discussion, subscripts I, II and III denote the three phases of the ITM system. Phase I denotes the time before the first time interface, phase II refers to the interval between the first and the second time interface and phase III indicates the state after the second time interface.

2.2.1 *Phase I: before the first time interface*

The expression of the forward propagating wave

$$\begin{aligned} p_{\text{I}}(x, t) &= \rho c \cos\big(k(x - ct)\big), \\ v_{\text{I}}(x, t) &= \cos\big(k(x - ct)\big), \end{aligned} \quad (17)$$

solves the 1-D acoustic wave equation (eq. 15), where p_{I} and v_{I} denote the pressure and velocity evolution before the first time interface. Again, k is the wavenumber of the propagating wave, the sound speed is $c = \sqrt{\lambda/\rho}$ and the wave propagates in a medium with an initial impedance $Z_{\text{I}} = \rho c$. Following D.A. Kopriva *et al.* (2021), the energy of the system in a periodic domain is defined as

$$E = \int_{-\frac{\pi}{k}}^{\frac{\pi}{k}} \left(\frac{1}{2\lambda}p^2 + \frac{1}{2}\rho v^2\right) \mathrm{d}x. \quad (18)$$

E is conserved for a system of conserved hyperbolic equations, if no external energy or force acts on it. For our analysis, E is constant until the system properties change at a time interface, and is also constant between time interfaces.

For Phase I, we obtain

$$E_{\text{I}} = \frac{\pi\rho}{k} \quad (19)$$

as the energy of the system before the activation of the time interface.

2.2.2 *Phase II: between the time interfaces*

An impedance contrast or interface in space causes a reflection of a wave (section 9.2 in R.J. LeVeque 2002) (Fig. 1a). To create a time interface, we scale the wave impedance by the factor n when the ITM is activated. At $t = t_{\text{ITM}}^-$, the Lamé parameter is changed to $\lambda_{II} = n^2\lambda_I$, which changes the impedance to $Z_{II} = nZ_I$. The solution to the correspondingly updated eq. (15) is (R.J. LeVeque 2002, section 2.8)

$$\begin{aligned} \frac{2p_{\text{II}}(x, t)}{c\rho} &= -(n-1)\cos\left(kx + cknt - (ckn + ck)t_{\text{ITM}}^-\right) \\ &\quad + (n+1)\cos\left(kx - cknt + (ckn - ck)t_{\text{ITM}}^-\right), \\ 2v_{\text{II}}(x, t) &= (n-1)\cos\left(kx + cknt - (ckn + ck)t_{\text{ITM}}^-\right) \\ &\quad + (n+1)\cos\left(kx - cknt + (ckn - ck)t_{\text{ITM}}^-\right), \end{aligned} \quad (20)$$

where p_{II} and v_{II} are the pressure and velocity for $t > t_{\text{ITM}}^-$. In each of the two pressure and velocity components, the first and second terms correspond to a converging and diverging part of the solution, respectively. For this choice of material change, the forward and backward propagating waves travel with a speed of nc, which is the coefficient of the time component in the cosine function, that is, the wave speed is multiplied by n. These solutions also indicate a phase shift of $(ckn \mp ck)t_{\text{ITM}}^-$ for a wave propagating forward and backward in response to the time interface, respectively, which is consistent with the observations and conclusions of V. Bacot *et al.* (2016). Using eq. (18), we can evaluate the system energy at $t > t_{\text{ITM}}^-$ as

$$E_{\text{II}} = \frac{1}{2}\frac{\left(1 + n^2\right)\pi\rho}{kn^2}. \quad (21)$$

Fig. 2(a) evaluates the energy ratio $E_{\text{II}}/E_{\text{I}}$ for different values of the time impedance factor n. Compared to the E_{I} reference state, the relative energy in the jolted system E_{II} decreases from large values at small $n < 1$ towards the asymptotic value of 0.5 for $n > 1$.

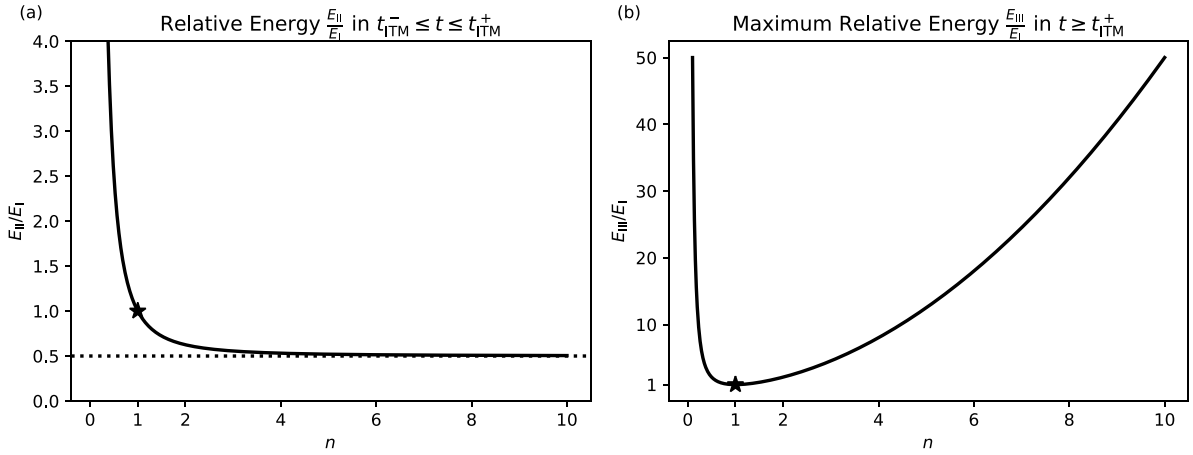

Figure 2. Energy ratios associated with time interfaces. The subscript I refers to the original state before the activation of a time interface, and states II and III are associated with the first and second time interface, respectively. The corresponding equations for E_I, E_{II} and E_{III} are eqs (19), (21) and (23), respectively, and n is the wave impedance factor. (a) The ratio E_{II}/E_I. The dashed line indicates the asymptotic value of 0.5. (b) The ratio E_{III}/E_I. The star indicates the neutral state associated with $n = 1$.

2.2.3 Phase III: after the ITM

At $t = t_{ITM}^+$, we change the material properties back to their initial state and solve eq. (15) again, which yields

$$\begin{aligned}
\frac{-4np_{III}(x,t)}{c\rho} &= (-n^2+1)\cos\left(kx+ckt-2ckt_{ITM}^- - (ckn+ck)\tau\right)\\
&\quad+(n^2-1)\cos\left(kx+ckt-2ckt_{ITM}^- + (ckn-ck)\tau\right)\\
&\quad+(n^2-2n+1)\cos\left(kx-ckt+(ckn+ck)\tau\right)\\
&\quad+(-n^2-2n-1)\cos\left(kx-ckt-(ckn-ck)\tau\right),\\
-4nv_{III}(x,t) &= (n^2-1)\cos\left(kx+ckt-2ckt_{ITM}^- - (ckn+ck)\tau\right)\\
&\quad+(-n^2+1)\cos\left(kx+ckt-2ckt_{ITM}^- + (ckn-ck)\tau\right)\\
&\quad+(n^2-2n+1)\cos\left(kx-ckt+(ckn+ck)\tau\right)\\
&\quad+(-n^2-2n-1)\cos\left(kx-ckt-(ckn-ck)\tau\right),
\end{aligned} \tag{22}$$

where $\tau = t_{ITM}^+ - t_{ITM}^-$, and p_{III} and v_{III} are pressure and velocity for $t > t_{ITM}^+$, respectively. Eq. (22) consists of four components, two components each travelling in the forward and reverse directions. This shows that an impedance discontinuity in time or an ITM generates a time-reversed wave component. The wave components exhibit a phase shift that depends on the ITM parameters. The final energy E_{III} depends on the parameters k, n and τ and is constrained by

$$\frac{\pi\rho}{k} \le E_{III} \le \frac{\pi\rho}{2k}\left(n^2+\frac{1}{n^2}\right). \tag{23}$$

This demonstrates that the application of an ITM leads to a change in the system energy. We can compare the maximum energy increase after the ITM to the initial state. We take the upper limit expression and plot the ratio E_{III}/E_I as a function of n. The minimum neutral value $E_{III}/E_I = 1$ is obtained at $n = 1$, and the system behaviour is therefore consistent with the observation by V. Bacot *et al.* (2016) that 'a temporal discontinuity in a homogeneous medium conserves momentum but not energy'.

2.3 The isotropic elastic wave equation

In Section 2.1, we have established the association between paired positive and negative eigenvalues and a time-reflected propagating plane wave in the presence of time interfaces using a general solution of a first-order wave equation. Next, we demonstrate this principle for an isotropic elastic medium to provide a basis for evaluating our numerical results, which involves the manipulation of P waves and S waves. To model the 3-D seismic wavefield, we use the velocity–stress formulation of the isotropic elastic wave equation. Using Einstein notation to indicate summation over repeated indices, these equations are

$$\begin{aligned}
&\frac{\partial\sigma_{ij}}{\partial t} - \lambda\delta_{ij}\frac{\partial v_k}{\partial x_k} - \mu\left(\frac{\partial v_i}{\partial x_j}+\frac{\partial v_j}{\partial x_i}\right) = 0,\\
&\rho\frac{\partial v_i}{\partial t} - \frac{\partial\sigma_{ij}}{\partial x_j} = 0,
\end{aligned} \tag{24}$$

where $\boldsymbol{\sigma}$ is the stress tensor, and consistent with eq. (14) the v_1, v_2 and v_3 are again the particle velocities in the x, y and z directions, respectively, λ and μ are the material dependent Lamé parameters, and ρ is density. The acoustic wave equation (eq. 14) emerges as a special case of eq. (24) for $\mu = 0$. In this case, all shear stresses $\sigma_{ij} = 0$ vanish, and all normal stresses are equal and equivalent to the pressure fluctuation $p = -\sigma_{ii}$. Eq. (24) matches the general linear PDE system eq. (1)

$$\frac{\partial\mathbf{q}}{\partial t} + \mathbf{A}\frac{\partial\mathbf{q}}{\partial x} + \mathbf{B}\frac{\partial\mathbf{q}}{\partial y} + \mathbf{C}\frac{\partial\mathbf{q}}{\partial z} = 0$$

for the state vector

$$\mathbf{q} = (\sigma_{11},\ \sigma_{22},\ \sigma_{33},\ \sigma_{12},\ \sigma_{23},\ \sigma_{31},\ v_1,\ v_2,\ v_3)^T. \tag{25}$$

The flux matrices **A**, **B** and **C** are 9×9 matrices, for example,

$$\mathbf{A} = \begin{pmatrix}
0 & 0 & 0 & 0 & 0 & 0 & -(\lambda+2\mu) & 0 & 0\\
0 & 0 & 0 & 0 & 0 & 0 & -\lambda & 0 & 0\\
0 & 0 & 0 & 0 & 0 & 0 & -\lambda & 0 & 0\\
0 & 0 & 0 & 0 & 0 & 0 & 0 & -\mu & 0\\
0 & 0 & 0 & 0 & 0 & 0 & 0 & 0 & 0\\
0 & 0 & 0 & 0 & 0 & 0 & 0 & 0 & -\mu\\
-\frac{1}{\rho} & 0 & 0 & 0 & 0 & 0 & 0 & 0 & 0\\
0 & 0 & 0 & -\frac{1}{\rho} & 0 & 0 & 0 & 0 & 0\\
0 & 0 & 0 & 0 & 0 & -\frac{1}{\rho} & 0 & 0 & 0
\end{pmatrix}. \tag{26}$$

We refer to M. Dumbser & M. Käser (2006) for the organization of these elements in the flux matrices, and for **B** and **C**. The eigenvalues of this system $(-c_p, -c_s, -c_s, 0, 0, 0, c_s, c_s, c_p)$ determine the propagation velocities of P waves and S waves, $c_p =$

$\sqrt{(\lambda+2\mu)/\rho}$ and $c_s = \sqrt{\mu/\rho}$, respectively. The corresponding eigenvector matrix is (M. Dumbser & M. Käser 2006)

$$\mathbf{R} = \begin{pmatrix} \rho c_p & 0 & 0 & 0 & 0 & 0 & 0 & \rho c_p \\ \frac{\lambda}{c_p} & 0 & 0 & 0 & 1 & 0 & 0 & \frac{\lambda}{c_p} \\ \frac{\lambda}{c_p} & 0 & 0 & 0 & 0 & 1 & 0 & \frac{\lambda}{c_p} \\ 0 & \rho c_s & 0 & 0 & 0 & 0 & \rho c_s & 0 \\ 0 & 0 & 0 & 1 & 0 & 0 & 0 & 0 \\ 0 & 0 & \rho c_s & 0 & 0 & 0 & \rho c_s & 0 & 0 \\ 1 & 0 & 0 & 0 & 0 & 0 & 0 & -1 \\ 0 & 1 & 0 & 0 & 0 & 0 & -1 & 0 \\ 0 & 0 & 1 & 0 & 0 & 0 & -1 & 0 & 0 \end{pmatrix}. \tag{27}$$

The eigenvector matrix depends only on the elastic material parameters ρ, λ and μ. This means that a material change at a time interface can create a situation in which the new eigenvectors differ compared to the eigenvectors before the time interface. Following the discussion in Section 2.1.2, we infer that the eigenvalues occur in pairs $\pm c_p$, $\pm c_s$, $\pm c_s$, and the zero eigenvalues do not contribute to propagating waves. Hence, a material interface that leads to a change in the eigenvectors leads to a corresponding reflected wavefield component.

This interaction of waves with material interfaces is a fundamental and well-studied aspect of wave propagation in general and seismic responses in particular (e.g. R.J. LeVeque 2002, section 9.2). These findings can be generalized to understand the wavefield response to time interfaces, which also exhibits splitting the propagation into time-reflected and transmitted components (Fig. 1b). As said, extending the single time interface to a time slab or instantaneous time mirror involves the restoration to the original medium parameters, that is, the phase I and phase III medium properties are the same (Section 2.2), which leads to the same wave speeds before and after the ITM as in the water tank experiment by V. Bacot *et al.* (2016). The extension of the 1-D solutions developed in this section to 3-D analytical ITM solutions for elastic waves excited by point or seismic sources can yield further observational targets and updated reference solutions for verification.

For anisotropic elastic materials, the structure of the associated eigenvector matrix $\mathbf{R}$ (e.g. J. de la Puente *et al.* 2007) governs the coupling of quasi-*P* waves and quasi-*S* waves. As a result, the *P* waves and *S* waves cannot be separately manipulated by scaling the respective impedances at a time interface, as shown for the isotropic medium. This suggests, as for other wave propagation phenomena, a more complex anisotropic medium response. Our well-resolved isotropic time interface models motivate an extended analysis of the response to an ITM in 3-D anisotropic elastic media using SeisSol (S. Wolf *et al.* 2020), which can also include simulations of refocusing Rayleigh surface wave behaviour in media with direction-dependent wave velocities (G. Hillers *et al.* 2016).

3 WAVEFIELD SIMULATIONS AND ITM IMPLEMENTATION IN SEISSOL

In this section, we first summarize the implementation of wavefield simulations in SeisSol (Section 3.1) and highlight the modifications necessary to incorporate the physics of time interfaces and ITMs. The code used in this study is publicly available, with details and reproducibility information provided in the **Data Availability** section. Readers primarily interested in the details of ITM-based wavefield manipulation may proceed directly to Section 3.2.

3.1 Overview of ADER-DG in SeisSol

SeisSol implements the ADER-DG method for elastic (M. Dumbser & M. Käser 2006), viscoelastic (M. Dumbser *et al.* 2007b; C. Uphoff & Bader 2016), anisotropic (J. de la Puente *et al.* 2007; S. Wolf *et al.* 2020) and poroelastic (J. de la Puente *et al.* 2008; S. Wolf *et al.* 2022) materials. In addition, it supports the coupling of acoustic and elastic domains (L. Krenz *et al.* 2023) along with a gravity boundary condition to model tsunamis (L. Krenz *et al.* 2021). SeisSol achieves high accuracy and utilizes local time-stepping, which allows for the computationally efficient exploration of complex wave propagation problems.

SeisSol solves the elastic wave equations written in first-order form as a linear hyperbolic PDE system, as given by eq. (1)

$$\frac{\partial \mathbf{q}}{\partial t} + \mathbf{A}\frac{\partial \mathbf{q}}{\partial x} + \mathbf{B}\frac{\partial \mathbf{q}}{\partial y} + \mathbf{C}\frac{\partial \mathbf{q}}{\partial z} = \mathbf{S}. \tag{28}$$

An additional source term is indicated by $\mathbf{S}$. The PDE system is solved using a high-order Discontinuous Galerkin (DG) method, which discretizes the domain into unstructured tetrahedral elements. In each element, the numerical solution is represented by space-dependent, orthogonal polynomial basis functions. The Arbitrary high-order DERivatives (ADER) method (V.A. Titarev & E.F. Toro 2002; M. Dumbser *et al.* 2008) is used for time integration. The resulting ADER-DG scheme combines a high-order element-local predictor with a corrector step that considers how the local solution depends on neighbour elements by solving Riemann problems. We refer to M. Dumbser & M. Käser (2006) and M. Dumbser *et al.* (2007b) for details of the ADER-DG method, and to C. Uphoff *et al.* (2017) and C. Uphoff & M. Bader (2020) for details of the ADER-DG implementation in SeisSol.

In each element k, the numerical solution for the nth time step is stored as a matrix $\mathbf{Q}_k^n$ of polynomial coefficients, with the quantities and polynomial basis functions as row and column dimensions of the matrix. The DG discretization in space turns eq. (28) into this equation for each element of the grid

$$\mathbf{D}^1 = \mathbf{M}^{-1}\left(\left(\mathbf{K}^{\xi}\right)^T\mathbf{Q}^n\mathbf{A}^* + \left(\mathbf{K}^{\eta}\right)^T\mathbf{Q}^n\mathbf{B}^* + \left(\mathbf{K}^{\zeta}\right)^T\mathbf{Q}^n\mathbf{C}^*\right), \tag{29}$$

where the mass matrix $\mathbf{M}$ and the stiffness matrices $\mathbf{K}^{\xi}$, $\mathbf{K}^{\eta}$ and $\mathbf{K}^{\zeta}$ result from the choice of the element-local basis functions. As we use orthogonal basis functions, $\mathbf{M}$ becomes diagonal. The matrices $\mathbf{A}^*$, $\mathbf{B}^*$ and $\mathbf{C}^*$ are linear combinations of the matrices $\mathbf{A}$, $\mathbf{B}$, and $\mathbf{C}$ from eq. (28), depending on the orientation of the element.

The first step in the ADER-DG scheme is a Taylor series expansion of the element-local space-time solution $\mathbf{I}$, for which we iterate over eq. (29) to compute the δth derivatives $\mathbf{D}^{\delta}$ for $0 \le \delta \le O$, with O the discretization order

$$\mathbf{D}^0 := \mathbf{Q}, \quad \mathbf{D}^{\delta+1} := \mathbf{M}^{-1}\left(\left(\mathbf{K}^{\xi}\right)^T\mathbf{D}^{\delta}\mathbf{A}^* + \left(\mathbf{K}^{\eta}\right)^T\mathbf{D}^{\delta}\mathbf{B}^* + \left(\mathbf{K}^{\zeta}\right)^T\mathbf{D}^{\delta}\mathbf{C}^*\right) \tag{30}$$

and then compute the space-time predictor as

$$\mathbf{I} = \sum_{\delta=0}^{O}\frac{\Delta t^{\delta+1}}{(\delta+1)!}\mathbf{D}^{\delta}, \tag{31}$$

which is referred to as the Cauchy-Kovalevskaya procedure (M. Dumbser & M. Käser 2006). From these space–time predictions

$\mathbf{I}$, an explicit update scheme for a time step can be derived

$$\mathbf{Q}^{n+1,*} = \mathbf{Q}^{n} + \mathbf{I}_{\text{vol}}(\mathbf{I}) - \mathbf{I}^{\text{local}}_{\text{surf}}(\mathbf{I}) - \mathbf{I}^{\text{surf}}_{\text{neigh}}\left(\mathbf{I}_{(i)}\right) + \mathbf{I}_{\text{src}}, \tag{32}$$

where the terms $\mathbf{I}_{\text{vol}}$ correspond to the volume discretization, the terms $\mathbf{I}^{\text{local}}_{\text{surf}}$ and $\mathbf{I}^{\text{global}}_{\text{surf}}$ to the numerical fluxes on the element surfaces, and $\mathbf{I}_{\text{src}}$ to the discretization of source terms. The volume term is computed as

$$\mathbf{I}_{\text{vol}}(\mathbf{I}) = \mathbf{M}^{-1}\left(\mathbf{K}^{\xi}\mathbf{I}\mathbf{A}^{*} + \mathbf{K}^{\eta}\mathbf{I}\mathbf{B}^{*} + \mathbf{K}^{\zeta}\mathbf{I}\mathbf{C}^{*}\right), \tag{33}$$

with all terms known from eq. (29). The surface contributions $\mathbf{I}^{\text{local}}_{\text{surf}}$ and $\mathbf{I}^{\text{neigh}}_{\text{surf}}$ are computed from contributions from all four faces of the tetrahedral cell

$$\begin{aligned}
\mathbf{I}^{\text{local}}_{\text{surf}}(\mathbf{I}) &= \frac{1}{|J|}\mathbf{M}^{-1}\left(\sum_{i=1}^{4}|S_i|\,\mathbf{F}^{-,i}\mathbf{I}\hat{\mathbf{A}}^{+}\right),\\
\mathbf{I}^{\text{neigh}}_{\text{surf}}\left(\mathbf{I}_{(i)}\right) &= \frac{1}{|J|}\mathbf{M}^{-1}\left(\sum_{i=1}^{4}|S_i|\,\mathbf{F}^{+,i,j,h}\mathbf{I}_{(\mathbf{i})}\hat{\mathbf{A}}^{-}_{(i)}\right),
\end{aligned} \tag{34}$$

where $|J|$ is the volume of the element and $|S_i|$ is the surface area of the ith face. The flux matrices $\mathbf{F}^{-,i}$ and $\mathbf{F}^{+,i,j_k,h_k}$ for each element k and for each face i depend on the choice of the basis functions and the relative position of the element with the respective neighbour (M. Dumbser & M. Käser 2006). $\hat{\mathbf{A}}^{+}_{k}$ and $\hat{\mathbf{A}}^{-}_{k(i)}$ are defined as $\hat{\mathbf{A}}^{+}_{k} = \frac{1}{2}\left(\hat{\mathbf{A}}_k + \left|\hat{\mathbf{A}}_k\right|\right)$ and $\hat{\mathbf{A}}^{-}_{k(i)} = \frac{1}{2}\left(\hat{\mathbf{A}}_{k(i)} - \left|\hat{\mathbf{A}}_{k(i)}\right|\right)$, where the notation of the absolute value of the flux matrix has the meaning of applying the absolute value operator to the given eigenvalues (M. Dumbser & M. Käser 2006).

We can write the source term $\mathbf{I}_{\text{src}}$ associated with a single point source

$$\mathbf{I}_{\text{src}} = |J|\left(\sum_{j=1}^{O}\omega_j s_{\text{ps}}(\tau_j)\right)\Psi(\xi_s), \tag{35}$$

where ω_j are integration weights, s_{ps} is the time-dependent component of the source term inside a mesh element, Ψ_k are space-dependent basis functions on the reference element and ξ_s is the location of the point source in the reference coordinate system. In this work we consider only point source simulations, but our SeisSol ITM can be generally applied to wavefields excited by extended finite sources. As none of the components required for the calculation of $\mathbf{I}_{\text{src}}$ depend on material properties, these do not need to be revised for the ITM implementation.

3.2 ITM wavefield manipulations in SeisSol

We implement an ITM for isotropic elastic waves by modifying the material properties to $\hat{\lambda}$, $\hat{\mu}$ and $\hat{\rho}$ for $t^{-}_{\text{ITM}} \le t \le t^{+}_{\text{ITM}}$. Body waves in isotropic elastic media propagate as a *P* wave or *S* wave, hence it is possible to reverse both waves together by changing the impedance or just one of the wave types without affecting the other. Here we analyse *P* wave and *S* wave scenarios, extending the previous work on ITM effects on elastic waves (K. Innanen 2018; K. Wapenaar *et al.* 2024). To change the impedance contrast, we can modify the density and keep the Lamé parameters constant or scale them in different proportions. In the following eqs (36) to (38), n denotes the impedance scaling factor.

3.2.1 Manipulating P waves and S waves

To reflect both waves, we modify the material parameters for the duration of the ITM from t^{-}_{ITM} to t^{+}_{ITM} as

$$\begin{aligned}
\hat{\lambda} &= n^2\lambda,\\
\hat{\mu} &= n^2\mu,\\
\hat{\rho} &= \rho.
\end{aligned} \tag{36}$$

This yields $\hat{c}_p = nc_p$, $\hat{c}_s = nc_s$, $\hat{Z}_p = nZ_p$ and $\hat{Z}_s = nZ_s$. The same n-scaling means that the ITM time steps are scaled by $1/n$ to maintain the stability condition discussed below (Section 3.2.4).

3.2.2 Manipulating P waves only

To reflect only *P* waves, we modify the material parameters such that only the *P* wave impedance changes without affecting the *S* wave impedance. We change the Lamé parameter λ and keep μ constant,

$$\begin{aligned}
\hat{\lambda} &= n^2\lambda,\\
\hat{\mu} &= \mu,\\
\hat{\rho} &= \rho.
\end{aligned} \tag{37}$$

We obtain $\hat{Z}_p = \sqrt{\rho(n^2\lambda + 2\mu)} \neq Z_p$ and $\hat{Z}_s = Z_s$, that is, only the *P*-wave impedance varies as intended. In this case, the *P*-wave velocity $c_p = \sqrt{(n^2\lambda + 2\mu)/\rho}$ is limited by nc_p whereas $\hat{c}_s = c_s$, and we can use the same time stepping as in the previous case.

3.2.3 Manipulating S waves only

Correspondingly, to reflect only *S* waves, we modify the material parameters such that only the *S*-wave impedance is changed without affecting the impedance of *P* waves. This is achieved by changing the density and the Lamé parameters,

$$\begin{aligned}
\hat{\lambda} &= \frac{\lambda + 2\mu}{n} - 2n\mu,\\
\hat{\mu} &= n\mu,\\
\hat{\rho} &= n\rho.
\end{aligned} \tag{38}$$

This yields $\hat{c}_p = c_p/n$, $\hat{c}_s = c_s$, $\hat{Z}_p = Z_p$ and $\hat{Z}_s = nZ_s$ during the ITM activation, hence only the *S*-wave propagation is affected. For the elastic simulations discussed in Section 4.2 we use $n > 1$ for the cases that involve *P*-wave manipulation and $n < 1$ for the last case where only the *S* wave is manipulated, with the corresponding effects on the time stepping.

3.2.4 ITM implementation

The ADER-DG update scheme, as summarized in Section 3.1, is formulated as a sequence of element-local matrix operations. As all matrices—with the exception of the quantities $\mathbf{Q}$—normally remain constant throughout a simulation, SeisSol pre-computes and stores all involved matrices during its setup phase. While $\mathbf{K}^{\xi}$, $\mathbf{K}^{\eta}$, $\mathbf{K}^{\zeta}$ and $\mathbf{M}$, as well as the flux matrices $\mathbf{F}^{-,i}$ and $\mathbf{F}^{+,i,j_k,h_k}$ depend on the discretization and on the geometry of the mesh elements, the matrices $\mathbf{A}^{*}$, $\mathbf{B}^{*}$, $\mathbf{C}^{*}$ depend directly on $\mathbf{A}$, $\mathbf{B}$, $\mathbf{C}$, which are again sensitive to the material parameters. Similarly, $\hat{\mathbf{A}}^{+}$ and $\hat{\mathbf{A}}^{-}_{(i)}$ contribute to the Riemann solution, which also depends on the local material parameters. Therefore, when the medium parameters change at a time interface, we recompute

all matrices $\mathbf{A}^*$, $\mathbf{B}^*$ and $\mathbf{C}^*$, as well as $\hat{\mathbf{A}}^+$ and $\hat{\mathbf{A}}^-_{(i)}$, for all DG elements.

As an explicit scheme, ADER time stepping must obey a Courant–Friedrichs–Lewy (CFL) condition (H. Lewy *et al.* 1928). For the elastic wave equation, the allowed time step size is inversely proportional to the largest wave speed c_p and proportional to the element size. SeisSol employs clustered local time stepping (LTS) (M. Dumbser & M. Käser 2006; A. Breuer *et al.* 2016), which groups elements with similar allowed time step sizes into clusters. These clusters are advanced with a uniform time step size, where the ratio between the time step sizes of two clusters is fixed, typically to powers of 2. Temporally changing material parameters for ITM requires that we also update the time step sizes to match the changed wave speeds. As mentioned in Sections 3.2.1 to 3.2.3, for the cases of reflecting both *P* wave and *S* wave, and for the case of reflecting only the *P* wave, it is sufficient to scale the time steps by the inverse impedance scaling factor $1/n$. For the case of manipulating only the *S*-wave propagation, we need to scale the time steps by $1/n$ if $n < 1$, but keep them constant for $n > 1$. Since ITM scaling does not change the ratios between time step sizes of elements and clusters, the LTS clusters can stay unchanged, and only the time steps for each LTS cluster need to be updated. ITM is thus compatible with the use of LTS.

To implement an ITM using an alternative numerical method, it suffices to modify the material properties and the relevant parameters for the time-step control. It is required to update the time-step sizes in response to the impedance scaling factor to ensure the CFL condition remains satisfied.

3.3 Numerical convergence test

We perform numerical convergence analysis to verify our implementation. We compare SeisSol synthetics of instantaneous time-mirrored acoustic waves to the analytical solution of a propagating planar acoustic wave discussed in Section 2.2. To quantify convergence, we compute the L^2 norm of the error of the v_1 velocity component of our numerical solution in response to a sinusoidal plane wave excitation with eq. (22) in Section 2.2. For this experiment we use $\tau = 0.01$ s and $n = 2$. We use a series of meshes consisting of uniformly sized tetrahedral elements in an 8 m^3 cubic domain. We increase the number of elements in each direction as 4, 8, 16, 32, 64, 128 and examine the error for polynomial orders $p \in \{1, 2, 3, 4, 5\}$. We expect a convergence order of $p+1$ for a polynomial order p used in the DG scheme (M. Käser & M. Dumbser 2006). The results are summarized in the decimal log–log plot in Fig. 3. The slope of the obtained relationships increases as expected with the polynomial order. For order $p = 5$, we observe an increase in error for the smallest grid size with 128 elements, which is due to reaching the limit of floating-point accuracy. We perform a linear fit of the error decimal logarithm and the grid size decimal logarithm to estimate the approximate convergence order obtained with our implementation. From the results in Table 1 we can conclude that our numerical discretization of the ITM converges with the expected order.

4 RESULTS FROM POINT SOURCE SIMULATIONS

We simulate the response of propagating wavefields that are excited by an impulse point source to time boundaries, first for an acoustic medium (Section 4.1) and then for an elastic case (Section 4.2). We use the half-space material parameters of the SISMOWINE WP2_LOH1 code validation benchmark (P. Moczo *et al.* 2006) that has been used to evaluate and compare the accuracy and performance of different wave propagation solvers. This benchmark scenario provides a reference for validating free-surface and internal interface wavefield responses. For the acoustic material we set $\mu = 0$ and adapt λ to yield the same *P*-wave speed as in the elastic case. We apply a standard seismic source time function at the centre of the domain. The source time function $\dot{S}$ is a Brune source time function (Fig. 4) that approximates an impulse force

$$\dot{S} = \frac{1}{T^2} t e^{-\frac{t}{T}}, \tag{39}$$

where t denotes time and T controls the width of the pulse approximating the duration of the source. This function is scaled by a seismic moment tensor that parametrizes a pressure source and a double couple source, or by a point force applied in the vertical direction. We use a conservatively large computational domain to avoid spurious reflections from non-perfectly absorbing boundaries. All 2-D wavefield images (Figs 5 to 10) are generated using the higher order output feature of SeisSol and are post-processed using an in-house visualization tool.

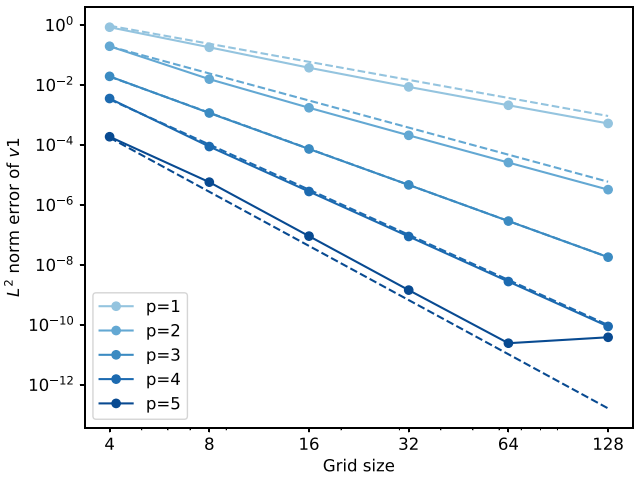

Figure 3. Convergence of the numerical SeisSol response to an instantaneous time mirror and the corresponding analytical plane wave solution for an acoustic medium (eq. 17). The grid size dependent L^2 norm of the differences in the v_1 velocity shows a positive dependence on the polynomial order p. The dashed lines show the theoretical convergence of $p + 1$ for polynomial order p.

Table 1. Convergence order versus polynomial order obtained from the convergence study of a propagating planar acoustic wave with ITM.

Polynomial order	1	2	3	4	5
Convergence order	2.13	3.15	4.00	5.03	5.77

4.1 The simulated response of an acoustic wavefield to time interfaces

We focus on the acoustic solution in response to a permanent change associated with a single time interface and compare key characteristics to theoretical predictions collected by K. Wapenaar *et al.* (2024) to corroborate our results. Then we discuss the refocusing behaviour associated with an ITM and connect the

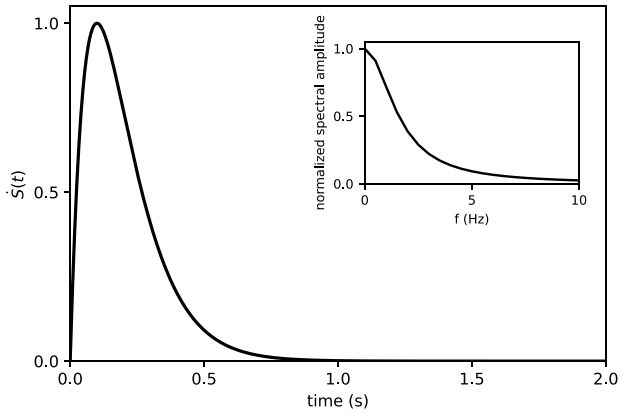

Figure 4. The source time function (eq. 39) used for the velocity impulse point source. The inset shows the normalized spectral amplitude of the source time function.

results to observations from established time-reversal applications. We first apply time interfaces to a P wave generated by a pressure impulse point source in an acoustic material. The initial material properties are

$$\begin{aligned} \rho &= 2700\,\mathrm{kg\,m^{-3}}, \\ \mu &= 0\,\mathrm{Pa}, \\ \lambda &= 9.72 \times 10^{10}\,\mathrm{Pa}, \end{aligned} \tag{40}$$

which lead to a P wave speed of $c_p = 6000\,\mathrm{m\,s^{-1}}$. The mesh used in this scenario resolves frequencies up to 10 Hz with these material properties (M. Käser *et al.* 2008). In the scenario with only one time interface, we resolve a higher frequency range due to the modified material parameters. The time interface parameters are

$$\begin{aligned} \tau &= 0.001\,\mathrm{s}, \\ n &= 10, \\ t^{-}_{\mathrm{ITM}} &= 5.0\,\mathrm{s}, \end{aligned} \tag{41}$$

where τ is the duration of the ITM, and n is the impedance scaling factor from eq. (36). These parameters result in the clean responses shown in Figs 1(b) and (c), 5 and 6.

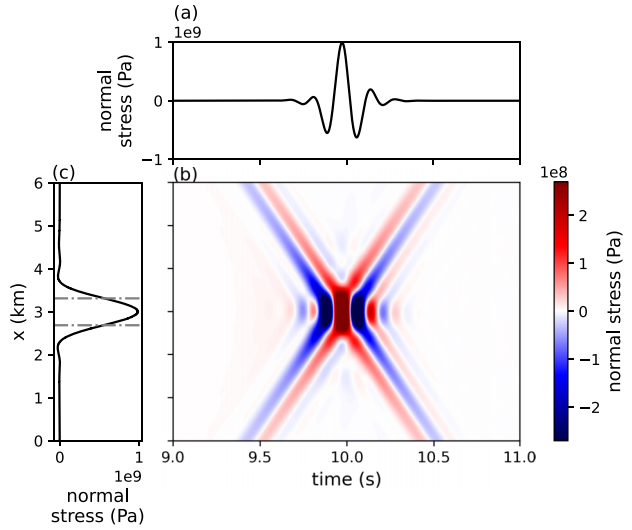

Figure 6. (a) Cross-section through the wavefield in panel (b) along the time axis at the location $x = 3$ km. (b) Space–time representation of the time-reversal collapse on the source location for an acoustic pressure wavefield excited by a pressure impulse moment tensor in response to an instantaneous time mirror activated at $t = 5$ s. The spatial and temporal refocusing occurs at $x = 3$ km and $t = 10$ s. The colour range is clipped. (c) Cross-section through the wavefield in panel (b) along the space axis at the refocusing time $t = 10$ s.

4.1.1 Reflection and transmission coefficients and frequency shift at a single time boundary

We first neglect phase III and the associated τ parameter in eq. (41) to compare features of our simulated single time interface responses to theoretical results. For a 1-D space boundary it is well known that the wavenumber of a planar wave changes according to $k_{\mathrm{II}} = k_{\mathrm{I}} c_{\mathrm{I}}/c_{\mathrm{II}}$ and the frequency is invariant, $\omega_{\mathrm{II}} = \omega_{\mathrm{I}}$. Correspondingly, for a time boundary, the wavenumber is invariant, $k_{\mathrm{II}} = k_{\mathrm{I}}$, but the frequency changes, $\omega_{\mathrm{II}} = \omega_{\mathrm{I}} c_{\mathrm{I}}/c_{\mathrm{II}}$ (K. Wapenaar *et al.* 2024; K. Wapenaar 2025). This means that for our time impedance factor $n = 10$, which yields a ten-fold increase in the

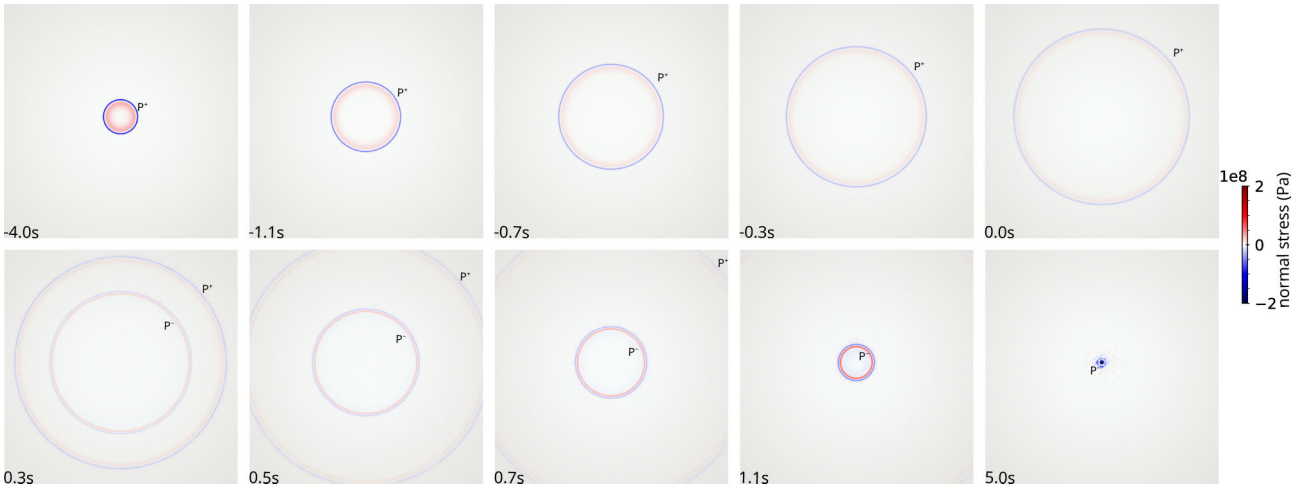

Figure 5. The response of an acoustic wavefield to an instantaneous time mirror activated at $t = 0.0$ s. The labels P^{+} and P^{-} indicate the diverging and converging wave, respectively. The panels show a 2-D section of the spherical wavefield in the y-z plane through the location of the pressure impulse moment tensor point source. The colour range is clipped.

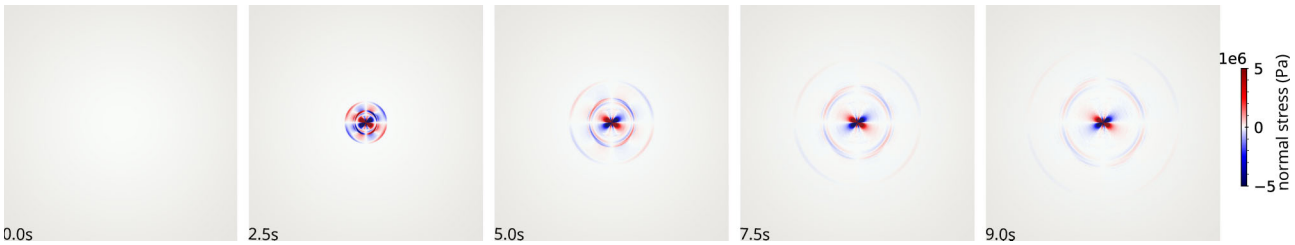

Figure 7. Illustration of an elastic wavefield in response to a moment tensor point source. The amplitudes of the propagating *P*-wave and *S*-wave decay away from the seismic moment tensor source, in contrast to the comparatively large-amplitude static near-field component. The colour range is clipped.

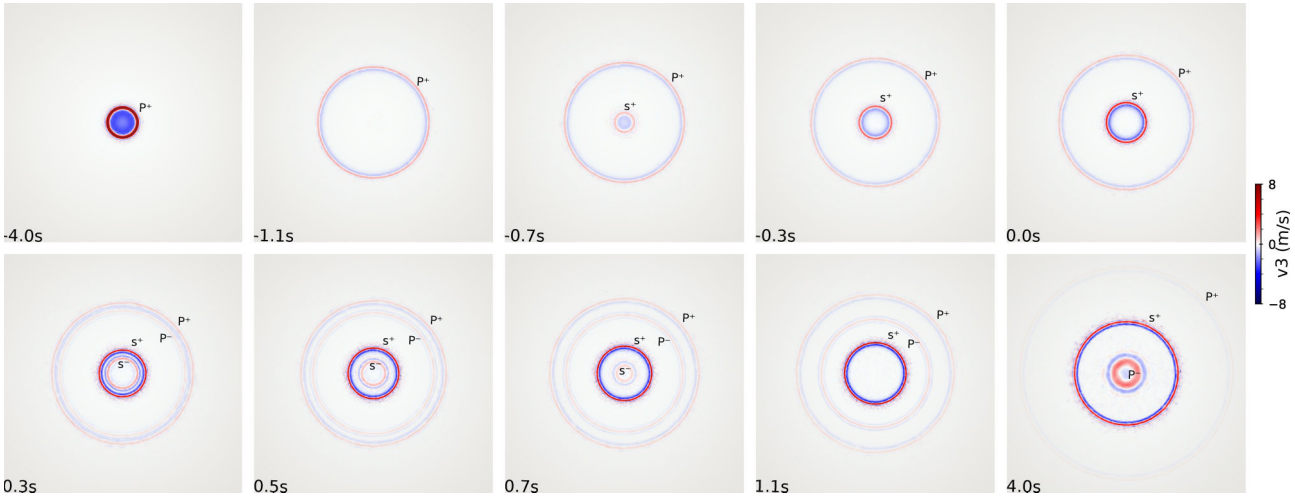

Figure 8. The response of an elastic wavefield to an instantaneous time mirror activated at $t = 0.0$ s. The intermittent change in the elastic parameters affects the *P* wave and the *S* wave. The superscripts + and − indicate the diverging and converging components, respectively. The panels show a 2-D section of the spherical wavefield in the *x*-*y* plane at $z = 28$ km in response to a vertical velocity impulse point force located at the origin. The colour range is clipped.

pressure wave speed, the frequencies of the reflected and transmitted waves are also expected to increase significantly. Similar to the established 1-D planar wave reflection and transmission coefficients R_x and T_x for a space boundary, K. Wapenaar *et al.* (2024) and K. Wapenaar (2025) developed R_t and T_t expressions for a time boundary in 1-D and 2-D, respectively,

$$R_t = \frac{1}{2}\left(\frac{\lambda_{\mathrm{I}}}{\lambda_{\mathrm{II}}} - \frac{c_{\mathrm{II}}}{c_{\mathrm{I}}}\right), \qquad T_t = \frac{1}{2}\left(\frac{\lambda_{\mathrm{I}}}{\lambda_{\mathrm{II}}} + \frac{c_{\mathrm{II}}}{c_{\mathrm{I}}}\right), \tag{42}$$

where λ is the bulk modulus, $c = c_p$, and the subscripts I and II refer again to the two phases before and after the time boundary, respectively, equivalent to the λ and $\hat{\lambda}$ notation in Section 3.2. This behaviour is illustrated in Fig. 1(b), where we can observe the incident 6 km s^{-1} wave speed up to $t < 5$ s (eq. 41), and then a ten-fold increase in the reflected and transmitted wave speeds for $t > 5$ s.

To analyse the frequency content we compute the Fourier amplitude spectra of 2 s long zero-padded waveforms of the incident, reflected and transmitted waves. The spectrum of the comparatively broad incident waveform (Fig. 1b) shows energy in the 0−10 Hz range and a peak around 1.5−2 Hz. The spectra associated with the significantly more narrow reflected and transmitted wavelets is correspondingly broader, with an observed peak around 15 Hz. This shift in the peak energy is thus in good agreement with the predicted shift of the central frequency by a factor of $\omega_{\mathrm{II}}/\omega_{\mathrm{I}} \approx c_{\mathrm{II}}/c_{\mathrm{I}} = 10$. This demonstrates that the wavenumber $k = \omega/c$ is preserved across a single time interface, which suggests that the time-boundary physics is sufficiently accurately resolved.

The theoretical reflection and transmission coefficients (eq. 42) for our material values (eq. 40) and $n = 10$ are $R_t = -4.995$ and $T_t = 5.005$, respectively. When we scale these values by the simulated incident amplitude of about −0.4, neglecting the order of magnitude of the considered normal stress values, we obtain estimates around +2.0 and −2.0, which are in good agreement with the simulated reflected and transmitted amplitudes of +1.9 and −1.8, respectively. These values are obtained for the broad-band signals but also for narrowband filtered waveforms using a Gaussian filter with 1.5 and 15 Hz central frequency. Again, the shift to higher frequencies suggests that the wavenumber k is preserved and the good estimates of the R_t and T_t coefficients demonstrate that our simulations of the response to a single time boundary are consistent with analytical plane wave model results. Residuals between the coefficients can be attributed to differing model assumptions: the analytical formulae assume 1-D and 2-D planar wave propagation (K. Wapenaar *et al.* 2024; K. Wapenaar 2025), whereas the numerical experiments employ fully 3-D numerical solutions for point sources.

4.1.2 Acoustic ITM refocusing and focal spot properties

The next step is the application of a second time boundary (Fig. 1c) after τ s that completes a time slab or the ITM. We

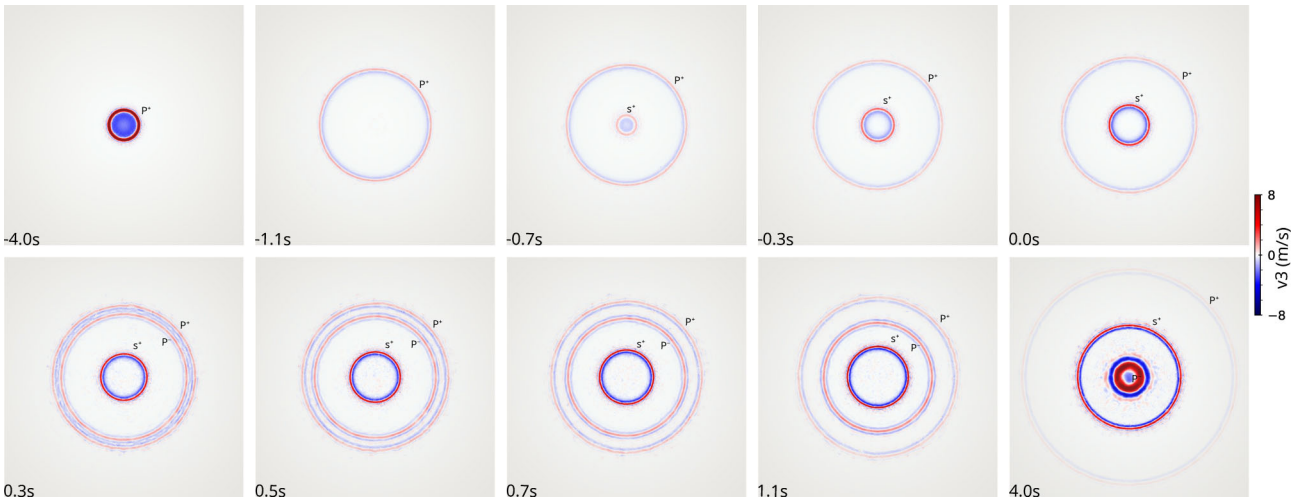

Figure 9. The response of an elastic wavefield to an instantaneous time mirror activated at $t = 0.0$ s. The intermittent change in the elastic parameters affects only the *P* wave. The superscripts + and − indicate the diverging and converging components, respectively. The panels show a 2-D section of the spherical wavefield in the *x*-*y* plane at $z = 28$ km in response to a vertical velocity impulse point force located at the origin. The colour range is clipped.

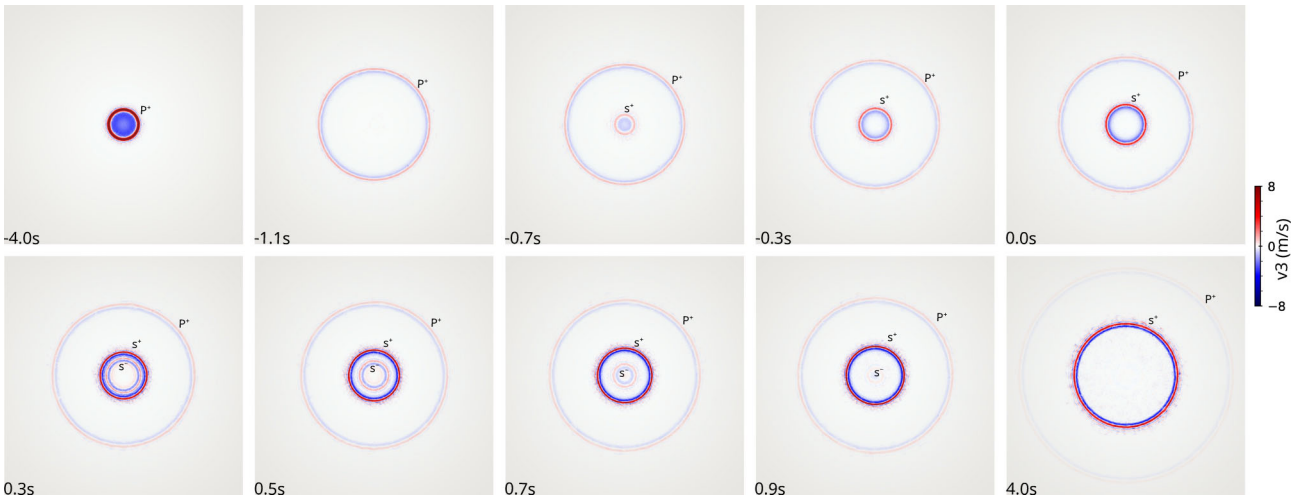

Figure 10. The response of an elastic wavefield to an instantaneous time mirror activated at $t = 0.0$ s. The intermittent change in the elastic parameters affects only the *S* wave. The superscripts + and − indicate the diverging and converging components, respectively. The panels show a 2-D section of the spherical wavefield in the *x*-*y* plane at $z = 28$ km in response to a vertical velocity impulse point force located at the origin. The colour range is clipped.

use a first example to demonstrate the effectiveness of our numerical solution again by connecting the properties of the simulated refocusing pattern or focal spot to results in the literature. The acoustic medium properties and time boundary values (eqs 40, 41) result in the 10 s long clean response obtained with the SeisSol ITM implementation illustrated in Fig. 5, where the visualization plane intersects the source location, and the indicated times are relative to t^-_{ITM}. The top five panels show the diverging P^+ wave that interacts with the ITM at $t = 0$ s. The $t = 0.3$ s panel shows the P^+ wave together with the new converging P^- wave that refocuses at $t = 5$ s. Note that the red-blue amplitude pattern of the P^+ and P^- waves illustrates the first-in-last-out symmetry associated with the ITM response (V. Bacot *et al.* 2016).

The spatiotemporal pressure field σ_{xx} is shown in an alternative illustration in Fig. 6(b). In the left part of the main panel it shows the converging wave that has been reflected by the ITM at $t = 5$ s before it refocuses at $t = 10$ s around the source position at 3 km and then diverges again in the right part. The slopes indicate the 6 km s^{-1} propagation speed. The corresponding cross-sections show the normal stress amplitude distributions along $x = 3$ km (Fig. 6a) and at $t = 10$ s (Fig. 6c). The large amplitude feature around the origin at the refocusing time is referred to as focal spot. The finite width of the focal spot is a consequence of the interacting converging and diverging parts of the wavefield. For seismic surface waves the focal spot is the time domain equivalent of the well known spatial autocorrelation (K. Aki 1957; G. Hillers *et al.* 2016; B. Giammarinaro *et al.* 2022; C. Tsarsitalidou *et al.* 2024). For a monochromatic body wave the focal spot shape is described by a sinc function, and its half-width or tip-curvature are a proxy for the local wavelength, and these relationships have been extensively utilized in acoustics and medical imaging applications (M. Fink 1997, 2006; S. Catheline *et al.* 2008; T. Gallot *et al.* 2011). The half-width is the width of the spot measured at half the peak amplitude, and it is an estimate of half a wavelength. In Fig. 6, the indicated half-width at the refocusing time $t = 10$ s is approximately 625 m. The ∼5 Hz central frequency of the wave after refocusing and

the 6 km s^{-1} local wave speed yield a wavelength of 1200 m, which agrees with our half-wavelength estimate. These results from the acoustic case relate our ITM response analysis to established time-reversal observations and corroborate the effectiveness and accuracy of our SeisSol simulations.

4.2 The simulated ITM response in an elastic medium

We extend the discussion from an acoustic to an isotropic elastic ITM response. We illustrate the general behaviour of 3-D waves in isotropic elastic media and discuss the three different possibilities of manipulating *P* waves and *S* waves, that is, we mirror the full body wavefield, and the *P* wave and the *S* wave separately. We first discuss the evanescent near-field component of the point source solution for moment tensor sources in elastic media. The non-propagating near-field term results from a moment tensor rate with a non-zero integral over the source duration (sections 4.2.3 and 2.6.2 in K. Aki & P.G. Richards 2002; H. Igel 2016). An example of this static near-field component is illustrated in the centre of the panels in Fig. 7 that show again the σ_{xx} component. In contrast to the propagating waves, this near-field component does not refocus in response to an ITM. In line with the energy increase observed in Section 2.2, however, the observed amplitudes of this static field also increase after an ITM. The near-field lobes as well as the amplitude distribution of the propagating *P* wave and *S* wave are controlled by the radiation pattern of the shear dislocation point source. As in Fig. 5 the visualization plane in Fig. 7 intersects the source location. Hence, we cannot reconstruct clean focal spots at the source location from the mirrored, converging wavefield as in Fig. 6 for elastic materials if the near-field effects are not filtered out. Instead, Figs 8 to 10 show the v_3 component of the simulated wavefields in the *y*-*z* plane at $x = 2$ km, which better illustrates the ITM response away from the source location at the origin and hence away from the large amplitudes in the near-field.

We apply an ITM to waves excited by point sources. We use the half-space material parameters of the LOH1 benchmark scenario

$$\begin{aligned} \rho &= 2700\,\mathrm{kg\,m^{-3}}, \\ \mu &= 3.24 \times 10^{10}\,\mathrm{Pa}, \\ \lambda &= 3.24 \times 10^{10}\,\mathrm{Pa}, \end{aligned} \tag{43}$$

which lead to *P* wave and *S* wave speeds of

$$\begin{aligned} c_p &= 6000\,\mathrm{m\,s^{-1}}, \\ c_s &= 3464\,\mathrm{m\,s^{-1}}, \end{aligned} \tag{44}$$

respectively. With these material parameters, the meshes we used can resolve up to 5 Hz in the domain of interest. The general ITM parameters are

$$\begin{aligned} \tau &= 0.01\,\mathrm{s}, \\ t^{-}_{\mathrm{ITM}} &= 9\,\mathrm{s}. \end{aligned} \tag{45}$$

For the two cases that involve *P*-wave manipulation we use the scaling factor $n = 10$, and for reflecting only the *S* wave we use $n = 0.1$. The respective ITM time steps are adjusted as explained in Section 3.2.4. To manipulate the wavefield for the three cases, the value of the impedance scaling factor n is applied in the corresponding eqs (36), (37) or (38). As before, these parameters yield the clean responses shown in Figs 8 to 10.

The panels in the top row in Fig. 8 show the diverging P^+ and S^+ waves in the visualization plane around $t = -4$ s and $t = -0.7$ s, respectively. At $t = 0.3$ s we can again discern the first-in-last-out symmetry of the amplitude pattern of the converging P^- and S^- waves that are created by the ITM at $t = 0$ s. All four waves continue to propagate, and around $t = 0.7$ s and $t = 4$ s the S^- wave and the P^- wave are about to 'exit' the visualization plane, respectively. Fig. 9 exhibits the same features at the same times, except that only a converging P^- wave emerges at $t = 0.3$ s in response to the ITM that leaves the *S*-wave propagation unaffected.

The wavefields in the top row panels in Fig. 10 are again identical to the solutions in Figs 8 and 9, but now only the S^- wave is generated and propagates back toward the centre, where it would refocus and diverge again. The *S*-wave manipulation is alternatively illustrated in the two wavefield representations in Fig. 11. Results in Fig. 11(a) show the space–time pattern along the *x*-axis at $y = 12$ km, $z = 40$ km, analogous to fig. 3(a) in V. Bacot *et al.* (2016). The profile extends radially away from the source at (12, 12, 68) km. The *P* wave propagates undisturbed but the converging S^- wave splits away from the diverging S^+ wave at the ITM activation. This highlights again the first-in-last-out symmetry, for example, at $t = 0.2$ s. The pattern also exhibits the ITM induced amplitude change of the transmitted S^+ wave, and the change in frequency content. The results in Fig. 11(b) are from the same simulation using an alternative time–space configuration for illustration, where the 20 km long profile ranges from (16, 12, 40) km to (36, 12, 40) km, that is, from 4 to 24 km relative to the source. This profile does not point radially away from the source at (12, 12, 68) km, which explains the different P^+ wave to S^+ wave amplitude ratio for $t < t^{-}_{\mathrm{ITM}} = 0$ s, the curved wave fronts, and the amplitude decay with distance. The illustration shows the phase change of the ITM affected *S* waveform, for example, by comparing the shapes of the S^+ wave and S^- wave at $x = 8$ km.

We observe a sensitivity in the simulated phase III amplitudes after t^{+}_{ITM} (Section 2.2), that is, the amplitudes of the manipulated waves in the lower row panels in Figs 8 to 10 and in Fig. 11, to our choice of the time impedance scaling factor n. Simulations with n values that are larger than $n = 10$ (eq. 45), or with values that are small compared to unity, lead to significantly larger amplitudes. These observations are compatible with the asymptotic results in eq. (23) illustrated in Fig. 2(b) that show an energy increase with n and $1/n$ in response to the ITM.

All results are obtained with empirically determined τ values in the range between 0.001 and 0.01 s to provide clean ITM responses for our demonstrations. The associated testing results suggest a sensitivity of the amplitude to variations in τ. This cannot, however, be linked to the analytical results in Section 2.2 that exhibit a τ dependence only in the cosine function argument of the reflected and transmitted planar acoustic waves (eq. 22). Adopting the interpretation of an ITM as the creation of secondary sources (V. Bacot *et al.* 2016), it can be hypothesized that the relation between the duration τ and the wavelet period, and thus its frequency content, controls the effective bandwidth of the time slab, that is, the excitation is potentially depleted of higher frequencies. To-be obtained analytical results for the 3-D elastic response to point sources, together with systematic numerical tests, can contribute to a comprehensive exploration of τ dependent energy scaling.

Our results convincingly illustrate the application of the ITM concept in an isotropic elastic medium. They exhibit the interesting phenomena to reverse either the full wavefield, or any one body wave component independently, by intermittently

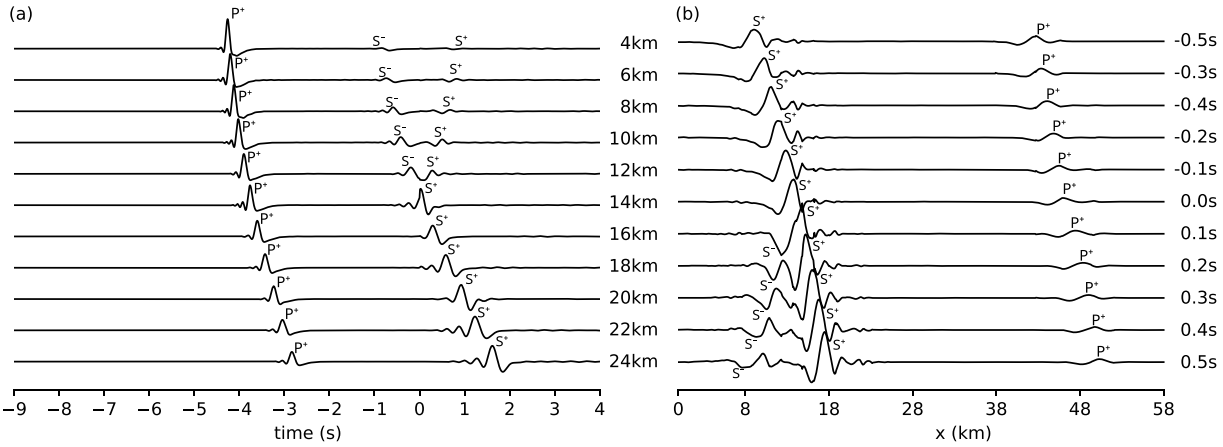

Figure 11. The response of an elastic wavefield to an instantaneous time mirror activated at $t = 0.0$ s using complementary space–time sampling configurations. The intermittent change in the elastic parameters affects only the *S* wave. (a) The wavefield along a 58 km long profile along the *x*-axis at $y = 12$ km, $z = 40$ km. The source is located at (12, 12, 68) km. (b) 13 s long seismograms along a 20 km section along the *x*-axis.

changing the medium parameters. The simulated responses demonstrate the robust implementation of ITM physics in SeisSol, but also highlight the potential for analytical developments for a more complete ITM energy partitioning theory.

5 DISCUSSION

The space–time analogy in wave propagation (Fig. 1) has led to growing interest in time-dependent manipulation of material properties, where instantaneous changes in elastic properties act as temporal boundaries. Similarities and differences in the responses to space and time-dependent changes are governed by the associated changes in boundary and initial conditions, respectively (V. Bacot *et al.* 2016; M. Fink & E. Fort 2017; K. Wapenaar *et al.* 2024; K. Wapenaar 2025). Our analytical and numerical analyses of the response of a 3-D elastic wavefield to a single time interface and to a time slab or instantaneous time mirror (ITM) in a 3-D elastic wave propagation framework using the open source code SeisSol advances seismic wavefield manipulations.

In this work, we investigate body-wave propagation in response to an intermittent change in the material properties of an isotropic homogeneous elastic full space. We consider instantaneous changes of the elastic parameters, and thus in the wave speeds and impedances, governed by a scaling factor n at a time interface, in contrast to periodic or other transient temporal variations. The numerical time step adaptation in response to this scaling enables an efficient implementation of alternative step-function protocols that involve consecutive jolts separated by periods that can be long compared to the short time-slab duration τ (K. Wapenaar *et al.* 2024).

An ITM of duration τ is constructed as a quick succession of two time interfaces, briefly altering and then restoring the original impedances. We establish analytical 1-D plane wave models of responses to time interfaces in acoustic media, providing insight into the system energy. We validate our simulated 3-D solutions using these analytical models. Using the properties of eigenvalues associated with the matrix structure of a general wave equation (Section 2) and of the 3-D elastic wave equation (Section 2.3) we establish a forward and backward propagating plane wave solution in response to a time interface that leads to a permanent medium change.

The plane wave approach is used for an acoustic 1-D case (Section 2.2) to build the diverging and converging solutions in response to an ITM, and these solutions yield expressions for the system energy budget that depend on n. It shows that the energy increases for all intermittent medium changes, for all n smaller and larger than unity (Fig. 2), which is compatible with non-steady-state energy considerations based on alternative formulations (K. Wapenaar *et al.* 2024) and thus corroborates the observation that a temporal discontinuity changes the energy in the system (V. Bacot *et al.* 2016). Importantly, the solutions for the forward and backward propagating plane waves provide the reference for validating the ITM responses.

We use the analytical solutions of the 1-D acoustic plane wave propagation to demonstrate the good convergence properties of our numerical implementation (Fig. 3) in the open-source software SeisSol that employs an ADER-DG scheme on unstructured tetrahedral meshes. For this demonstration we force a sinusoidal propagating plane wave. The convergence test establishes the positive dependence of the L^2 norm on the spatial discretization and on the polynomial order. We emphasize that the L^2 norm measures the agreement of both diverging and converging wave components in response to the ITM activation. This corroborates the numerical ITM implementation for the manipulation of a 3-D elastic wavefield excited by a point source, for which we do not derive a corresponding reference solution. These results also imply the accuracy of ITM manipulated wavefields excited by finite sources.

A first key result from our 3-D acoustic point source simulations involves refocusing in response to an ITM. The collapsing acoustic wavefield yields a large-amplitude feature at the source location (Fig. 6). The properties of this focal spot are controlled by the local medium properties, which supports a wide range of imaging approaches that are complementary to tomography (S. Catheline *et al.* 2008, 2013; T. Gallot *et al.* 2011; B. Giammarinaro *et al.* 2022; C. Tsarsitalidou *et al.* 2024). Here the good agreement between our P wave speed estimates of $c_P = 6.25$ km s^{-1} based on the narrow-band filtered focal spot width (Fig. 6) and the controlled velocity $c_P = 6.00$ km s^{-1} supports again the notion of an accurate wave physics implementation in

SeisSol. The validity of the implementation is further supported by our estimates of the reflected and transmitted wave amplitudes across a single time interface that are in good agreement with the plane wave predictions by K. Wapenaar *et al.* (2024). This exercise also corroborates the scaling of the frequency content of the reflected and transmitted signals with the impedance scaling factor n, which differs fundamentally from the constant frequency content across an interface in space. In agreement with the water tank results by V. Bacot *et al.* (2016) the 2-D slices of the ITM manipulated wavefield (Fig. 5) illustrate the first-in-last-out symmetry of the amplitude pattern that differs from the first-in-first-out reflections at a space interface and at a time-reversal mirror. For the elastic case the large-amplitude static near-field component (Fig. 7) prohibits the width measurements of P wave and S wave focal spots. This is inconvenient for numerical focal spot imaging studies (B. Giammarinaro *et al.* 2022, 2024), but it can be mitigated using appropriate filters. Another key result of our implementation is the independent control of P waves and S waves using a selective ITM impedance variation (Figs 9 and10). The intriguing possibility of separating converging P waves from S waves highlights the greater diversity of elastic wavefield phenomena compared to ITM responses for electromagnetic or acoustic propagation. This can support the development of efficient numerical strategies for synthetic wavefield manipulations.

Electromagnetic fields are comparatively easy to manipulate by changing the admittance, in contrast to time-dependent variations of Earth materials. Seismic wavefields can be engineered using resonator arrays that can lead to effective seismic metamaterials with the potential to reduce seismic hazard (A. Colombi *et al.* 2016; D. Mu *et al.* 2020). Backward propagation plays an important role in adjoint tomography (J. Tromp *et al.* 2005) and in constraining seismic source locations (G.A. McMechan 1982; A. Rietbrock & F. Scherbaum 1994; D. Gajewski & E. Tessmer 2005; C. Larmat *et al.* 2006) and earthquake rupture processes (F. Krüger & M. Ohrnberger 2005; E. Kiser & G. M. Ishii 2017). These backpropagation workflows can potentially benefit from the efficient ITM generation of converging wavefields presented in this study. Domain decomposition methods couple low-resolution results in a large background medium with high-resolution wave propagation in a target subvolume for computational efficiency (P. Moczo *et al.* 1997; V. Monteiller *et al.* 2012). Time-reversal solutions have been used to inject or re-generate wavefields across the spatial boundary of the subvolume (Y. Masson *et al.* 2013). The analogy between space and time interfaces, together with the connection between time-reversal approaches and ITMs, suggests that the boundary sources can also be realized with ITM physics (V. Bacot *et al.* 2016).

The software SeisSol supports simulations of dynamic rupture as well as seismic, acoustic and gravity wave propagation in complex geometries and heterogeneous geomaterial properties (e.g. L. Krenz *et al.* 2023; T. Taufiqurrahman *et al.* 2023; K.H. Palgunadi *et al.* 2024). Community use of this open-source code is supported by frequent training workshops and tutorials (M.A. Denolle *et al.* 2025). Our ITM implementation extends the computational framework to simulate and explore the effects of time-varying properties of Earth materials at different scales. SeisSol has demonstrated its utility in challenging Earth Science multiphysics simulations that involve rapid distributed material changes associated with large earthquakes (e.g. Z. Niu *et al.* 2025b). Our solutions can be adapted to help constrain damage-related radiation associated with local failure processes (Y. Cheng *et al.* 2021; Z. Niu *et al.* 2025a), by accounting for the rapid changes in the elastic moduli that can occur during brittle deformation episodes in an earthquake source region (e.g. Y. Ben-Zion & C.G. Sammis 2003; T. Mitchell & D. Faulkner 2009).

Properties of the focal spot or the spatial autocorrelation field are indicators of the local wave speed. Numerical focal spot syntheses based on analytical solutions (S. Catheline *et al.* 2008), time-reversal mirrors (B. Giammarinaro *et al.* 2022) or correlations of scattered or diffuse wavefields (S. Catheline *et al.* 2013; B. Giammarinaro *et al.* 2024) are essential for method development including robustness and sensitivity analyses. The noise correlation and Green's function analogy (A. Derode *et al.* 2003) supports seismic dense array-based Rayleigh wave focal spot imaging (G. Hillers *et al.* 2016; C. Tsarsitalidou *et al.* 2024) that has not been explored systematically for anisotropic media except for initial observations of azimuthally variable surface wave speeds (G. Hillers *et al.* 2016). Focal spot synthesis by time-reversal mirroring of Rayleigh waves in an azimuthally anisotropic medium (G. Hillers *et al.* 2023) is challenging because of the accurate implementation of the boundary conditions. Together with the implementation of anisotropic elastic parameters in SeisSol (S. Wolf *et al.* 2020; G. Hillers *et al.* 2023) the ITM engine can be used to synthesize focal spots in media with direction-dependent properties, provided that the refocusing field is separated from the static near-field components.

Additional physics and configurations leading to richer phenomena have been investigated in other domains and applications. These include ITM in inelastic, heterogeneous and dissipating materials (J.G.M. Besten *et al.* 2021; C.T. Wu *et al.* 2022), time reflection and refraction (J. Mendonça & P. Shukla 2002), incidence angle dependence of reflection and transmission (J.B. Pendry 2008) and wave conversions associated with oblique reflections (K. Innanen 2018). Future extensions of our work can explore these concepts and applications for seismic wavefields.

6 CONCLUSIONS

We analyse wavefield behaviour in time-varying media that are spatially uniform. Our eigenvector-based analytical solutions model acoustic waves at time interfaces. These models provide a framework for energy balance estimates in jolted systems and are used as reference solutions for our numerical convergence tests. These tests illustrate the effectiveness of the employed SeisSol ADER-DG solution for the numerical simulation of wavefield phenomena in media that are heterogeneous in space and time. Our simulated 3-D elastic wavefields in response to an instantaneous time mirror showcase the possibility to manipulate the complete wavefield but also to tune the propagation of the P waves and S waves independently, which emphasizes the richness in seismic wave propagation compared to ITM responses for electromagnetic or acoustic waves.

ACKNOWLEDGMENTS

This work is inspired by a presentation by M. Fink at the Institut des Sciences de la Terre, University Grenoble Alpes, in 2016. We thank D. Schneller for implementing the higher order

output used for the wavefield visualizations (funded by KONWIHR, Competence Network for Scientific High Performance Computing in Bavaria). We thank the editor C. Tape and the reviewers J. Aichele and Y. Masson for comments that helped to improve the manuscript. VK, LK, AAG and MB acknowledge funding provided (as part of the EuroHPC Joint Undertaking) for the ChEESE-2P cluster of excellence by Horizon Europe (grant agreement No. 101093038) and by the German Federal Ministry of Research, Technology and Space. GH acknowledges support from the Research Council of Finland (Flagship of Advanced Mathematics for Sensing Imaging and Modelling grant 359182 and grant 322421). AAG acknowledges additional support from Horizon Europe (DT-GEO, grant number 101058129 and Geo-INQUIRE, grant number 101058518), the National Science Foundation (NSF grant numbers CRESCENT EAR-2225286, MTMOD EAR-2121568, LCCF-CSA OAC-2323116, QUAKEWORX OAC-2311208), the National Aeronautics and Space Administration (NASA 80NSSC20K0495) and the Statewide California Earthquake Center (SCEC projects 25259, 25313, 25341). The CSC IT Center for Science, Finland, grand challenge Project Number 2003841 provided access to the CSC Mahti computational infrastructure.

DATA AVAILABILITY

All simulation files to reproduce the point source simulations with acoustic and elastic materials can be found at https://doi.org/10.5281/zenodo.15877555. The Sismowine LOH1 benchmark scenario is described in http://www.sismowine.org/model/WP2_LOH1.pdf (Moczo et al. 2006). Details of the implementation of point sources in SeisSol are discussed in https://seissol.readthedocs.io/en/latest/point-source-older-implementation.html. Details about installing and running SeisSol can be found at https://seissol.readthedocs.io/en/latest/build-overview.html. SeisSol is available at https://github.com/SeisSol/SeisSol/.

REFERENCES

Aki, K., 1957. Space and time spectra of stationary stochastic waves, with special reference to microtremors, *Bull. Earthq. Res. Inst.,* **35,** 415–456.

Aki, K. & Richards, P.G., 2002. *Quantitative Seismology,* 2nd edn, University Science Books.

Bacot, V., Labousse, M., Eddi, A., Fink, M. & Fort, E., 2016. Time reversal and holography with spacetime transformations, *Nature Phys.,* **12**(10), 972–977.

Ben-Zion, Y. & Sammis, C.G., 2003. Characterization of Fault Zones, *Pure appl. Geophys.,* **160**(3), 677–715.

Besten, J. G.M., Marks, B. & Einav, I., 2021. Reversing and amplifying elastic waves in inelastic granular media, *Granular Matter,* **24**(1) doi:10.1007/s10035-021-01180-9.

Breuer, A., Heinecke, A. & Bader, M., 2016. Petascale local time stepping for the ADER-DG finite element method, in *2016 IEEE International Parallel and Distributed Processing Symposium (IPDPS),* pp. 854–863, IEEE, Chicago.

Castanheira-Pinto, A., Alves-Costa, P., Godinho, L. & Amado-Mendes, P., 2018. On the application of continuous buried periodic inclusions on the filtering of traffic vibrations: a numerical study, *Soil Dyn. Earthq. Eng.,* **113,** 391–405.

Catheline, S., Benech, N., Brum, J. & Negreira, C., 2008. Time reversal of elastic waves in soft solids, *Phys. Rev. Lett.,* **100,** 064301

Catheline, S., Souchon, R., Rupin, M., Brum, J., Dinh, A.H. & Chapelon, J.-Y., 2013. Tomography from diffuse waves: Passive shear wave imaging using low frame rate scanners, *Appl. Phys. Lett.,* **103**(1), 014101.

Cheng, Y., Wang, X., Zhan, Z. & Ben-Zion, Y., 2021. Isotropic source components of events in the 2019 Ridgecrest, California, earthquake sequence, *Geophys. Res. Lett.,* **48**(18) doi:10.1029/2021GL094515.

Colombi, A., Colquitt, D., Roux, P., Guenneau, S. & Craster, R.V., 2016. A seismic metamaterial: the resonant metawedge, *Sci. Rep.,* **6**(1), 27717

de la Puente, J., Käser, M., Dumbser, M. & Igel, H., 2007. An arbitrary high-order discontinuous Galerkin method for elastic waves on unstructured meshes - IV. Anisotropy, *Geophys. J. Int.,* **169**(3), 1210–1228.

de la Puente, J., Dumbser, M., Käser, M. & Igel, H., 2008. Discontinuous Galerkin methods for wave propagation in poroelastic media, *Geophysics,* **73**(5), T77–T97.

Denolle, M.A. *et al.*, 2025. Training the Next Generation of Seismologists: Delivering Research-Grade Software Education for Cloud and HPC Computing Through Diverse Training Modalities, *Seism. Res. Lett.,* **96,** 3265–3279.

Derode, A., Larose, E., Tanter, M., de Rosny, J., Tourin, A., Campillo, M. & Fink, M., 2003. Recovering the Green's function from field-field correlations in an open scattering medium (L), *J. acoust. Soc. Am.,* **113**(6), 2973–2976.

Dijckmans, A., Ekblad, A., Smekal, A., Degrande, G. & Lombaert, G., 2016. Efficacy of a sheet pile wall as a wave barrier for railway induced ground vibration, *Soil Dyn. Earthq. Eng.,* **84,** 55–69.

Dumbser, M. & Käser, M., 2006. An arbitrary high-order discontinuous Galerkin method for elastic waves on unstructured meshes—II. The three-dimensional isotropic case, *Geophys. J. Int.,* **167**(1), 319–336.

Dumbser, M., Käser, M. & Toro, E.F., 2007a. An arbitrary high-order discontinuous Galerkin method for elastic waves on unstructured meshes - V. Local time stepping and p-adaptivity, *Geophys. J. Int.,* **171,** 695–717.

Dumbser, M., Käser, M. & Toro, E.F., 2007b. An arbitrary high-order Discontinuous Galerkin method for elastic waves on unstructured meshes–V. Local time stepping and p-adaptivity, *Geophys. J. Int.,* **171**(2), 695–717.

Dumbser, M., Balsara, D.S., Toro, E.F. & Munz, C.-D., 2008. A unified framework for the construction of one-step finite volume and discontinuous Galerkin schemes on unstructured meshes, *J. Comput. Phys.,* **227**(18), 8209–8253.

Ekström, G., Abers, G.A. & Webb, S.C., 2009. Determination of surface-wave phase velocities across USArray from noise and Aki's spectral formulation, *Geophys. Res. Lett.,* **36**(18) doi:10.1029/2009GL039131.

Evans, L.C., 2010. *Partial Differential Equations: Second Edition, Vol. 19 R of Graduate Series in Mathematics,* American Mathematical Society.

Fink, M., 1997. Time reversed acoustics, *Phys. Today,* **50**(3), 34–40.

Fink, M., 2006. Time-reversal acoustics in complex environments, *Geophysics,* **71**(4), SI151–SI164.

Fink, M. & Fort, E., 2017. From the time-reversal mirror to the instantaneous time mirror, *Eur. Phys. J. Special Topics,* **226**(7), 1477–1486.

Gabriel, A.-A. *et al.*, 2025. *SeisSol, Version v1.3.2 [software],* Zenodo. Available at: https://doi.org/10.5281/zenodo.15685917.

Gajewski, D. & Tessmer, E., 2005. Reverse modelling for seismic event characterization, *Geophys. J. Int.,* **163**(1), 276–284.

Galiffi, E., Xu, G., Yin, S., Moussa, H., Ra'di, Y. & Alù, A., 2023. Broadband coherent wave control through photonic collisions at time interfaces, *Nature Phys.,* **19**(11), 1703–1708.

Gallot, T., Catheline, S., Roux, P., Brum, J., Benech, N. & Negreira, C., 2011. Passive elastography: shear-wave tomography from physiological-noise correlation in soft tissues, *IEEE Trans. Ultrason. Ferroelectr. Frequency Control,* **58**(6), 1122–1126.

Gérardin, B., Laurent, J., Legrand, F., Prada, C. & Aubry, A., 2019. Negative reflection of elastic guided waves in chaotic and random scattering media, *Sci. Rep.,* **9**(1), 2135.

Giammarinaro, B., Tsarsitalidou, C., Hillers, G., de Rosny, J., Seydoux, L., Catheline, S., Campillo, M. & Roux, P., 2022. Seismic surface wave

focal spot imaging: numerical resolution experiments, *Geophys. J. Int.,* **232**(1), 201–222.
Giammarinaro, B., Tsarsitalidou, C. & Hillers, G., 2024. Investigating the lateral resolution of the surface wave focal spot imaging technique using two-dimensional acoustic simulations, *C. R. Géosci.,* **356** 41–57
Guéguen, P., Bard, P.-Y. & Cha´vez-Garci´a, F.J., 2002. Site-city seismic interaction in Mexico City–like environments: an analytical study, *Bull. seism. Soc. Am.,* **92**(2), 794–811.
Heinecke, A. *et al.*, 2014. Petascale high order dynamic rupture earthquake simulations on heterogeneous supercomputers, in *SC14: Proceedings of the International Conference for High Performance Computing, Networking, Storage and Analysis,* pp. 3–14, IEEE Press, New Orleans.
Hillers, G., Roux, P., Campillo, M. & Ben-Zion, Y., 2016. Focal spot imaging based on zero lag cross-correlation amplitude fields: Application to dense array data at the San Jacinto fault zone, *J. geophys. Res.: Solid Earth,* **121**(11), 8048–8067.
Hillers, G. *et al.*, 2023. Resolution of elastic, anelastic, and anisotropic medium properties using surface wave focal spot imaging, in American Geophysical Union *AGU Fall Meeting Abstracts,* pp. S11B–04.
Igel, H., 2016. *Computational Seismology: A Practical Introduction,* Oxford Univ. Press.
Innanen, K., 2018. Space-time boundary reflections in elastic media, in *CREWES Research Report — Volume 30*. Available at: https://www.crewes.org/Documents/ResearchReports/2018/CRR201825.pdf
Käser, M., Castro, C., Hermann, V. & Pelties, C., 2010. SeisSol–A software for seismic wave propagation simulations, in *High Performance Computing in Science and Engineering, Garching/Munich 2009,* pp. 281–292, Springer.
Kiser, E. & Ishii, M., 2017. Back-projection imaging of earthquakes, *Annu. Rev. Earth Planet. Sci.,* **45,** 271–299.
Kopriva, D.A., Gassner, G.J. & Nordström, J., 2021. Stability of discontinuous Galerkin spectral element schemes for wave propagation when the coefficient matrices have jumps, *J. Sci. Comput.,* **88**(1), 3.
Krenz, L., Uphoff, C., Ulrich, T., Gabriel, A.-A., Abrahams, L.S., Dunham, E.M. & Bader, M., 2021. 3D acoustic-elastic coupling with gravity: the dynamics of the 2018 Palu, Sulawesi earthquake and tsunami, in *Proceedings of the International Conference for High Performance Computing, Networking, Storage and Analysis, SC '21,* Association for Computing Machinery, New York, NY, USA
Krenz, L., Wolf, S., Hillers, G., Gabriel, A. & Bader, M., 2023. Numerical Simulations of Seismoacoustic Nuisance Patterns from an Induced *M* 1.8 Earthquake in the Helsinki, Southern Finland, Metropolitan Area, *Bull. seism. Soc. Am.,* **113**(4), 1596–1615.
Krüger, F. & Ohrnberger, M., 2005. Tracking the rupture of the M_w = 9.3 Sumatra earthquake over 1,150 km at teleseismic distance, *Nature,* **435**(7044), 937–939.
Käser, M. & Dumbser, M., 2006. An arbitrary high-order discontinuous Galerkin method for elastic waves on unstructured meshes—I. The two-dimensional isotropic case with external source terms, *Geophys. J. Int.,* **166**(2), 855–877.
Käser, M., Hermann, V., &, 2008. Quantitative accuracy analysis of the discontinuous Galerkin method for seismic wave propagation, *Geophys. J. Int.,* **173**(3), 990–999.
Larmat, C., Montagner, J.-P., Fink, M., Capdeville, Y., Tourin, A. & Clévédé, E., 2006. Time-reversal imaging of seismic sources and application to the great Sumatra earthquake, *Geophys. Res. Lett.,* **33**(19), doi:10.1029/2006GL026336.
LeVeque, R.J., 2002. *Finite Volume Methods for Hyperbolic Problems, Cambridge Texts in Applied Mathematics,* Cambridge Univ. Press.
Lewy, H., Friedrichs, K. & Courant, R., 1928. Über die partiellen Differenzengleichungen der mathematischen Physik, *Math. Ann.,* **100,** 32–74.
Lin, F.-C., Ritzwoller, M.H. & Snieder, R., 2009. Eikonal tomography: surface wave tomography by phase front tracking across a regional broad-band seismic array, *Geophys. J. Int.,* **177**(3), 1091–1110.
Masson, Y., Cupillard, P., Capdeville, Y. & Romanowicz, B., 2013. On the numerical implementation of time-reversal mirrors for tomographic imaging, *Geophys. J. Int.,* **196**(3), 1580–1599.
McMechan, G.A., 1982. Determination of source parameters by wavefield extrapolation, *Geophys. J. Int.,* **71**(3), 613–628.
Mendonça, J. & Shukla, P., 2002. Time refraction and time reflection: two basic concepts, *Phys. Scripta,* **65**(2), 160.
Mitchell, T. & Faulkner, D., 2009. The nature and origin of off-fault damage surrounding strike-slip fault zones with a wide range of displacements: a field study from the Atacama fault system, northern Chile, *J. Struct. Geol.,* **31**(8), 802–816.
Moczo, P., Bystrický, E., Kristek, J., Carcione, J.M. & Bouchon, M., 1997. Hybrid modeling of *P-SV* seismic motion at inhomogeneous viscoelastic topographic structures, *Bull. seism. Soc. Am.,* **87**(5), 1305–1323.
Moczo, P., Ampuero, J., Kristek, J., Galis, M., Day, S. & Igel, H., 2006. The European network SPICE code validation, in *Geophysical Research Abstracts, Vol. 8, 05760,* European Geosciences Union, Abstract 1607-7962/gra/EGU06-A-05760. Available at: https://scispace.com/pdf/the-european-network-spice-code-validation-3btlirklj9.pdf
Monteiller, V., Chevrot, S., Komatitsch, D. & Fuji, N., 2012. A hybrid method to compute short-period synthetic seismograms of teleseismic body waves in a 3-D regional model, *Geophys. J. Int.,* **192**(1), 230–247.
Mu, D., Shu, H., Zhao, L. & An, S., 2020. A review of research on seismic metamaterials, *Adv. Eng. Mater.,* **22**(4), 1901148
Niu, Z., Gabriel, A.-A. & Ben-Zion, Y., 2025a. Delayed dynamic triggering and enhanced high-frequency seismic radiation from brittle rock damage in 3D dynamic rupture simulations, *J. geophys. Res.: Solid Earth,* **130**(9), e2025JB031632
Niu, Z., Gabriel, A.-A., Wolf, S., Ulrich, T., Lyakhovsky, V. & Igel, H., 2025b. A discontinuous Galerkin method for simulating 3D seismic wave propagation in nonlinear rock models: verification and application to the M_w 7.8 2015 Gorkha, Nepal Earthquake, *J. geophys. Res.: Solid Earth,* **130**(7), e2025JB031378.
Pacheco-Peña, V. & Engheta, N., 2020. Antireflection temporal coatings, *Optica,* **7**(4), 323–331.
Palgunadi, K.H., Gabriel, A.-A., Garagash, D.I., Ulrich, T. & Mai, P.M., 2024. Rupture Dynamics of Cascading Earthquakes in a Multiscale Fracture Network, *J. geophys. Res.: Solid Earth,* **129**(3), doi:10.1029/2023JB027578.
Pendry, J.B., 2008. Time reversal and negative refraction, *Science,* **322**(5898), 71–73.
Pilz, M. *et al.*, 2024. Wind turbines as a metamaterial-like urban layer: an experimental investigation using a dense seismic array and complementary sensing technologies, *Front. Earth Sci.,* **12,** doi:10.3389/feart.2024.1352027.
Pu, X. & Shi, Z., 2020. Broadband surface wave attenuation in periodic trench barriers, *J. Sound Vib.,* **468,** 115130
Rietbrock, A. & Scherbaum, F., 1994. Acoustic imaging of earthquake sources from the Chalfant Valley, 1986, aftershock series, *Geophys. J. Int.,* **119**(1), 260–268.
Roux, P. *et al.*, 2018. Toward seismic metamaterials: The METAFORET Project, *Seismol. Res. Lett.,* **89**(2A), 582–593.
Shapiro, N.M., Campillo, M., Stehly, L. & Ritzwoller, M.H., 2005. High-Resolution Surface-Wave Tomography from Ambient Seismic Noise, *Science,* **307**(5715), 1615–1618.
Taufiqurrahman, T., Gabriel, A.-A., Li, D., Ulrich, T., Li, B., Carena, S., Verdecchia, A. & Gallovič, F., 2023. Dynamics, interactions and delays of the 2019 Ridgecrest rupture sequence, *Nature,* **618**(7964), 308–315.
Tirole, R. *et al.*, 2023. Double-slit time diffraction at optical frequencies, *Nature Phys.,* **19**(7), 999–1002.
Titarev, V.A. & Toro, E.F., 2002. ADER: Arbitrary high order Godunov approach, *J. Sci. Comput.,* **17**(1–4), 609–618.
Tromp, J., Tape, C. & Liu, Q., 2005. Seismic tomography, adjoint methods, time reversal and banana-doughnut kernels, *Geophys. J. Int.,* **160**(1), 195–216.

Tsarsitalidou, C., Hillers, G., Giammarinaro, B., Boué, P., Stehly, L. & Campillo, M., 2024. Long period Rayleigh wave focal spot imaging applied to USArray data, *J. geophys. Res.: Solid Earth,* **129**(5), e2023JB027417.

Uphoff, C. & Bader, M., 2016. Generating high performance matrix kernels for earthquake simulations with viscoelastic attenuation, in *2016 International Conference on High Performance Computing Simulation (HPCS),* pp. 908–916, IEEE, Innsbruck, Austria.

Uphoff, C. & Bader, M., 2020. Yet another tensor toolbox for discontinuous Galerkin methods and other applications, *ACM Trans. Math. Softw.,* **46**(4), 34:1–34:40.

Uphoff, C., Rettenberger, S., Bader, M., Madden, E.H., Ulrich, T., Wollherr, S. & Gabriel, A.-A., 2017. Extreme scale multi-physics simulations of the tsunamigenic 2004 Sumatra Megathrust Earthquake, in *Proceedings of the International Conference for High Performance Computing, Networking, Storage and Analysis, SC '17,* pp. 21:1–21:16, ACM, New York, NY, USA.

Wapenaar, K., 2025. Green's functions, propagation invariants, reciprocity theorems, wave-field representations and propagator matrices in two-dimensional time-dependent materials, *Proc. R. Soc. A: Math. Phys. Eng. Sci.,* **481**(2307), 20240479.

Wapenaar, K., Aichele, J. & van Manen, D.-J., 2024. Waves in space-dependent and time-dependent materials: a systematic comparison, *Wave Motion,* **130,** 103374

Wolf, S., Gabriel, A.-A. & Bader, M., 2020. Optimization and local time stepping of an ADER-DG scheme for fully anisotropic wave propagation in complex geometries, in *Computational Science - ICCS 2020, no. 12139 in Lecture Notes in Computer Science,* pp. 32–45, Springer.

Wolf, S., Galis, M., Uphoff, C., Gabriel, A.-A., Moczo, P., Gregor, D. & Bader, M., 2022. An efficient ADER-DG local time stepping scheme for 3D HPC simulation of seismic waves in poroelastic media, *J. Comput. Phys.,* **455,** 1–29.

Wu, C.T., Nobre, N.M., Fort, E., Riley, G.D. & Costen, F., 2022. Tailoring instantaneous time mirrors for time reversal focusing in absorbing media, *IEEE Trans. Antennas Propag.,* **70**(10), 9630–9640.